Department of Physics and Astronomy

University of Heidelberg

Bachelor thesis

in Physics

submitted by

Roxana-Adela Chira

born in Temeschburg (Romania)

2011

Characterisation of Infrared Dark Clouds

This bachelor thesis has been carried out by Roxana-Adela Chira

at the

Max-Planck-Institute for Astronomy in Heidelberg

under the supervision of

Priv.-Doz. Dr. Henrik Beuther

Fakultät für Physik und Astronomie

Ruprecht-Karls-Universität Heidelberg

Bachelorarbeit

Im Studiengang Physik

vorgelegt von

Roxana-Adela Chira

geboren in Temeschburg (Rumänien)

2011

Charakterisierung infraroter Dunkelwolken

Die Bachelorarbeit wurde von Roxana-Adela Chira

ausgeführt am

Max-Planck-Institute für Astronomie in Heidelberg

unter der Betreuung von

Priv.-Doz. Dr. Henrik Beuther

Abstract

The Initial Mass Function (IMF) is a distribution showing how numerous stars with specific masses are. It is observed that there is a peak of the IMF between 0.1-1 M$\odot$. Thus, low-mass stars like our sun are more common than high-mass stars. But high-mass stars contain the majority of the galaxy's luminosity. So, they are the only visible objects in other galaxies which can be effectively observed. Thus, the understanding of high-mass star formation is not only important for the generel understanding of star formation, but also for the understanding of galaxy structures.

In a crude view, high-mass star formation is similar to the formation of low-mass stars. But, there are some other factors needed to be taken into account like the need of very massive cloud cores and a higher accretion rate. There are different scenarios which shall help us to simulate the formation stages. But for computing a realistic scenario and comparing the results with real observations, one has to know the initial conditions of star-forming regions.

My studies concentrate on the early stages of infrared dark clouds (IRDCs) which are supposed to be star-forming regions, but do not contain any protostellar objects, yet. To learn more about the initial conditions of IRDCs, 220 candidates with strong contrast profile in the infrared were chosen. Based on the infrared observations of the Midcourse Space Experiment (MSX), a catalogue of possible IRDCs have been created containing all regions with a significant constrast - being defined as constrast = (background - image) / background - to the bright background. The 220 candidate IRDCs have been observed in ammonia with the 100m-telescope in Effelsberg. With these data, I was able to calculate the temperature and column density of ammonia, and the distances and virial masses of the IRDCs. I used the Atacama Pathfinder Experiment (APEX) Telescope Large Area Survey of the Galaxy (ATLASGAL) in dust emission at 870 μm for deriving the gas masses and the virial parameter of the sample. This survey observed a great part of the Galactic Midplane in submillimeter wavelengths and is, thus, helpful for estimating initial conditions like gas masses, column densities, density structures, as well as for studying large-scale morphologies.

The IRDCs' rotation temperatures are averaged about 15 K, linewidths between 0.5 and 2.5 km s^{-1}, column densities in order of 10^{15} cm^2 g^{-1}. Thus, they are colder and less turbulent than more evolved regions of high-mass star formation. The virial masses are between 100 and a few 1000 $M_\odot$ being sufficient for forming high-mass stars. The virial parameter is defined as ratio between the gravitional and kinetic energy of an source. The parameters of the sample IRDCs are in order of 1. This indicates that the sources are approximately in virial equilibrium.

In my thesis, I want to present these results in more detail, interpret them in the astrophysical context and compare the parameters with previous observations of high-mass protostellar objects (HMPOs) supposing to be the next evolutionary stage in high-mass star formation.

Zusammenfassung

Die anfängliche Massenfunktion (englisch: Initial Mass Function, IMF) zeigt eine Verteilung, die angibt, wie viele Sterne bestimmter Massen existieren. Das Maximum dieser Verteilung liegt zwischen 0,1 und 1 $M_{\odot}$. Also gibt es mehr masseärmere Sterne als massereichere. Allerdings machen diese massereichen Sterne den Hauptteil der Leuchtkraft der Galaxie aus. So kommt es, dass sie die einzigen Objekte sind, die man in anderen Galaxien effektiv beobachten kann. Deshalb ist es nicht nur für das allgemeine Verständnis der Sternentstehung wichtig, zu verstehen, wie diese Sterne entstehen, sondern auch für das Verständis von Strukturen aller Galaxien.
Grob gesehen entstehen massereiche Sterne ähnlich wie masseärmere. Allerdings gibt es ein paar Faktoren, die zusätzlich berücksichtigt werden müssen, zum Beispiel die Notwendigkeit sehr massereicher Molekülwolken and hoher Akkretionsraten. Es gibt verschiedene Szenarien, die uns bei der Simulation der einzelnen Entwicklungsschritte helfen sollen. Um realistische Simulationen schreiben und diese mit Beobachtungen vergleichen zu können, benötigt man gute Kenntnisse der Anfangsbedingungen der Regionen, in denen Sterne entstehen.
Meine Untersuchungen konzentrieren sich auf die anfänglichen Stadien der infraroten Dunkelwolken (englisch: infrared dark clouds, IRDCs), welche man für Geburtstätten von Sternen hält, die allerdings noch keine protostellaren Objekte enthalten. Um mehr über die Anfangsbedingungen dieser IRDCs zu lernen, wurden 220 sehr kontrastreiche Kandidaten aus ausgewählt. Basierend auf den Beobachtungen im Infraroten durch das Midcource Space Experiment (MSX) wurde ein Katalog möglicher IRDCs kreiert, welcher alle Regionen erhält, deren Kontrast, welcher als Kontrast = (Hintergrund - Bild) / Hintergrund definiert ist, signifikant gegenüber dem hellen Hintergrund ist. Die 220 IRDC Kandidaten wurden mit dem 100m-Effelsberg Radio Teleskop im Ammoniak beobachtet. Mit diesen Daten war es mir möglich, die Rotationstemperaturen und Säulendichten von Ammoniak, sowie die Entfernungen und Virialmassen der IRDCs zu berechnen. Zusätzlich verwendete ich die Daten des Atacama Pathfinder Experiment (APEX) Telescope Large Area Survey of the Galaxy (ATLASGAL), welcher die galaktische Ebene in der Staubemission bei 870 μm kartierte, um die Gasmassen und Virialparameter dieser Auswahl bestimmen zu können. ATLASGAL hat einen großen Teil der galaktischen Mittelebene in submillimeter Wellenlängen beobachtet und ist somit hilfreich zum Bestimmen der Anfangsbedingungen wie Gasmassen, Säulendichten, Dichtestrukturen, sowie für Untersuchungen ganzer großflächiger Morphologien.
Die IRDCs haben im Mittel Rotationstemperaturen von etwa 15 K, Linienbreiten zwischen 0,5 und 2,5 km s^{-1}, Säulendichten in der Größenordnung von 10^{15} cm^2 g^{-1}. Damit sind sie kälter und weniger turbulent als die weiter entwickelten Regionen, in denen massereiche Sterne entstehen. Die Virialmassen liegen zwischen 100 und ein paar 1000 $M_{\odot}$, was ausreicht, um massereiche Sterne entstehen zu lassen. Der Virialparameter ist definert als das Verhältnis zwischen gravitativer und kinetischer Energie einer Quelle. Die Parameter der ausgewählten IRDCs liegen im Bereich von etwa 1. Dies deutet darauf hin, dass die Quellen annähernd im virialen Gleichgewicht sind.
In meiner Arbeit möchte ich diese Ergebnisse detaillierter präsentieren, in einem astrophysikalischen Kontext interpretieren und die Parameter mit einer Auswahl massereicher protostellarer Objekte (englisch: high-mass protostellar objects, HMPOs; gelten als nächstes Stadium in der Entwicklung massereicher Sterne) einer früheren Beobachtung vergleichen.

Contents

1 Introduction

The Initial Mass Function (IMF) being sketched in figure 1.1 shows that there are clearly more low-mass stars than high-mass ones. Therefore, it is not suprising that the formation and evolution of low-mass stars are better understood than those of more massive stars. The studies of high-mass stars and their formation are important, because these massive stars emit the majority of galaxy's luminosities. That is why they are the only observable objects in other galaxies.

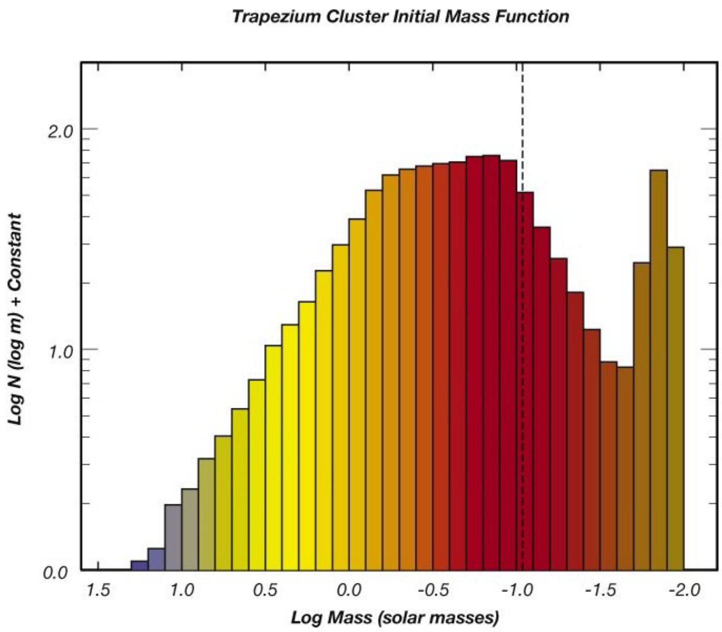

Figure 1.1: Initial Mass Function: This IMF is a distribution describing how numerous stars of masses between 0.01 and 1.5 $M_\odot$ are. Its peak is located between 0.1 and 1 $M_\odot$. To higher masses the distribution follows a power law (Muench et al., 2002).

In addition to that, high-mass stars are important for the life cycles of all stars. They contain a lot of energy and angular momentum which they are able to blow out into space via stellar winds, molecular outflows, ultraviolet radiation and supernova explosions. With those, partially violent processes, high-mass stars influence the interstellar chemistry as well. In this context, it is interesting to learn more about the birth-rates, distributions and timescales of massive stars and the correlation with these quantities for low-mass stars (i.e. for extragalactic star formation).
In this chapter, I want to give a short introduction in our current understanding of star formation and show the similarities and differences between low- and high-mass star formation. My own studies concentrate on the earliest stages of high-mass star formation supposed to be found in so called Infrared Dark Clouds (IRDCs). From a catalogue containing candidate IRDCs based

on the data Midcourse Space Experiment (MSX), there have been 220 IRDCs selected. Their spectra have been observed with the Effelsberg radio telescope. The bandwidth was chosen to be between 23.65 GHz and 24.15 GHz making it possible to observe the ammonia (1,1)- and (2,2)-inversion lines (at 23694.495 MHz and 23722.633 MHz) in one spectrum and analysing their hyperfine structures. With those, it was possible to study some parameters of the IRDCs' initial conditions which are going to be presented and discussed in the next chapters.

1.1 Star Formation

1.1.1 Low-Mass Star Formation

Already in the 18^{th} century, there were considerations by Kant (1755) and Laplace (1796) of stars forming via gravitational collapse of interstellar medium. But it took astronomers and astrophysicsts a long time to build up a *standard theory* of star formation. With this standard theory, it is possible to explain the formation of stars with less than 8 $M_{\odot}$, no matter whether they are isolated or embedded in clusters.

It is supposed that there are clouds of interstellar medium which form dense cores. These cores are in hydrostatic equilibrium for a long time (about 10^6 years). The gravity wanting the cores to collapse is balanced by turbulences, magnetic fields and thermal pressure. But if gravity becomes strong enough to overcome its counterparts in one of those cores, they start to collapse probably in an inside-out fashion. That means, that in the first step just a little part of the later star's mass (about 10%) forms the first central protostar. The remaining 90% are accreted from the surrounding envelope, so that the protostellar's luminosity is gained by accretion shocks. During this process an accretion disk and bipolar outflow forms around the protostar. In this time, the protostar is embedded within the optical thick envelope, and therefore not directly observable yet. While the accretion process continues, the envelope clears up, until it is optical thin enough for the protostar being observable. In the Herztsprung-Russell diagram (HRD), the line on which the protostars are observable for the first time is called birth line (see fig. 1.2). From now on, the further development of the (pre-main sequence) stars are tracked in the HRD.

The pre-main sequence is the time between the end of main accretion and the beginning of hydrogen burning. In this part of evolution, the star's central temperature is not high enough to burn hydrogen efficiently. But the envelope is too empty to feed the star as in the protostellar phase. Hence, the pre-main sequence star starts to contract. The gravitational potential is converted into thermal energy and luminosity, until the central temperature reaches about 10^7 K being sufficiently for burning hydrogen. In dependency of its mass the pre-main sequence star tracks through the HRD, until it reaches the Zero-Age Main Sequence (ZAMS) representing the start of hydrogen burning. This is the real "birth" of a star. Until the CNO cycle at the end of the stars' life times, the luminosiy is now gained by nuclear reactions.

1.1.2 High-Mass Star Formation

The described formation scenario above works only for stars with less than 8 $M_{\odot}$. If a forming star becomes more massive, other effects being negligible for low-mass stars have to be considered.

For example, high-mass stars start their hydrogen burning while they are still accreting mass from their envelope. Thus, the problem of radiative pressure arises, because this additional pressure is able to slow the accretion process down or even stop it in one-dimensional simulations.

Also the accretion rate itself is a problem. The rate for low-mass stars is in the order 10^{-6} - 10^{-5} $M_{\odot}$/yr being too low for forming a high-mass star in the given timescales.

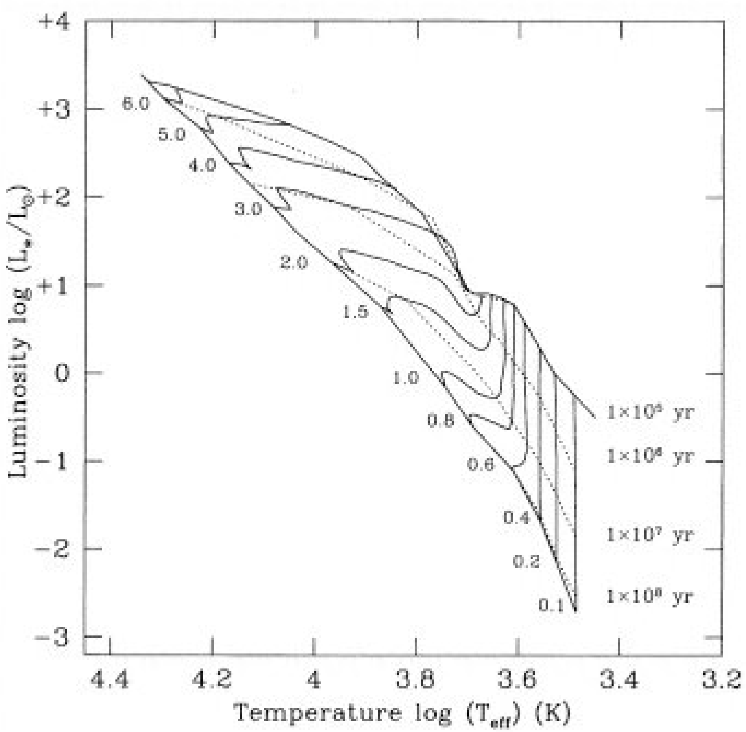

Figure 1.2: Theoretical pre-main sequence tracks in der HRD. In dependency of the stars' masses the tracks have been simulated and ploted. The dotted lines represent selected isochrones. All tracks start on the (upper) birth line and end on the (lower) Zero-Age Main Sequence (ZAMS) (Pallai et al., 1999).

There are two popular ansatzes to solve these problems. The first one is the coalescene scenario. It says that in clusters with high stellar densities ($\sim 10^8$ pc^{-3}), it may be possible that protostellar clumps, being formed in the low-mass fashion, collide and merge (Bonnell et al., 1998; Stahler et al., 2000; Zinnecker et al., 2002).
The second scenario adapts the standard theory for low-mass star formation and increases the parameters, like accretion rates (Jijina et al., 1996; Norberg et al., 2000; Tan et al., 2002; Wolfire et al., 1987; Yorke, 2002). That means, that instead of an accretion rate of 10^{-6}-$10^{-5} M_{\odot}$/yr, there would be rates of the order 10^{-4} - 10^{-3} $M_{\odot}$/yr neccesary to form a massive star. Also, disks, which transporting the mass to the protostar, have to form.
For learning more about the real high-mass star formation, it is neccesary to collect more information about the individual stages of star formation. In this thesis, I concentrate on the very earliest stage: the Infrared Dark Clouds.

1.1.3 Molecular Clouds

The space between stars and star systems is not empty, but filled with gas, dust and cosmic rays being united in the concept of the interstellar medium (ISM). Besides those main components, the ISM contains also electromagnetic radiation, a gravitational field and a magnetic field. Almost all matter (99%) is in gas phase and includes about 70% hydrogen (atomic and molecular), 28% helium, and 2% heavier elements (Ward-Thompson et al., 2011).

The ISM can be classified into four phases depending on their initial conditions. The Hot Ionised Medium (HIM) contain diffuse, hot ($\sim 10^4$ K), ionised gas being formed by radiation, stellar winds (i.e. by young massive stars) and supernova remnants. Regions of warm ($10^3 - 10^4$ K) and partially ionised gas are called Warm Ionised Medium (WIM). This is the form of gas filling the majority of the Galaxy's disc. The most common techniques to observe these two kinds of ISM are the Hα emission and pulsar dispersion. Latter uses the boardering of an otherwise sharp pulsar pulse. By this, the electron density between the pulsar and the observer can be measured. In opposite to the HIM, HI-regions are clouds of cold (50-100 K), neutral regions of atomic gas and are observed in the HI 21 cm line emission. Finally, there are the large regions of cold (20-50 K), dense, and molecular gas, the so called *dark clouds* or *molecular clouds*. An example is shown in fig. 1.3.

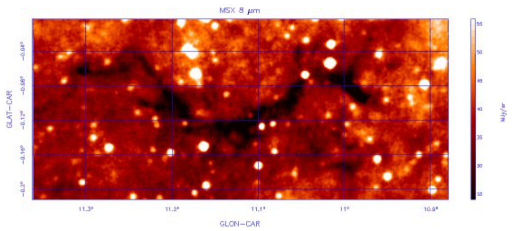

Figure 1.3: Image of the IRDC G11.11-00.11 in 8 μm from MSX (URL: S. J. Carey). The optically thick region hides the background stars behind.

The largest of these molecular clouds are called *Giant Molecular Clouds* (GMCs). They have sizes of 20 - 100 pc and masses of the order 10^4 - 10^6 $M_\odot$. The average local densities of hydrogen are about $4 \cdot 10^3$ - $1.2 \cdot 10^4$ cm^{-3} and the average temperatures are in the order 15 - 20 K. Consequently, they are observed at infrared and radio wavelengths (more details in ch. 1.3). There are also weak magnetic fields with field strengths of the order of a few 10 μG.
Although molecular hydrogen is the most common component in GMCs, dust is very important for the heating and cooling processes within the clouds (stabilising the temperature and keeping the clouds balanced), and for the interstellar chemistry itself. The fraction of dust in the ISM is just 1%, but it is enough to let the cloud be optical thick. Hence, not only visible and infrared light is blocked, but also ultraviolet radiation which would be able to destroy molecules.
The dust grains' surface is also needed as catalyser to form molecules. These reactions are additionally supported by turbulences within the molecular clouds. With a velocity dispersion of 2 - 3 km s^{-1} they are highly supersonic (average sound speed is about 0.2 km s^{-1}) and are supposed to be an important counterpart of gravity for keeping a cloud in balance.
But GMCs are not uniform. Within these large structures smaller, denser cores form supposed to be locations of star formation. These *Infrared Dark Clouds* (IRDCs) have sizes of 0.25 - 0.5 pc, masses of the order 100 - 1000 $M_\odot$, mean densities of 10^5 cm^{-3} and temperatures of about 16 K. They also contain some high-density molecular line tracers like ammonia being helpful for analysing the initial conditions (more details in ch. 2). In my studies, I have concentrated on the analysis of two ammonia inversion lines in the spectra of 220 IRDCs. The technical way how to find and catalogue IRDCs will be descriped in chapter 1.4, as well as the selection criteria with which the sample of IRDCs has been chosen.

1.2 Interstellar Ammonia

Until today, about 160 molecules have been tracked in the ISM being listed up in table 1.1.

Number of Atoms										
2	3	4	5	6	7	8	9	10	11	12+
H_2	C_3	c-C_3H	C_5	C_5H	C_6H	CH_3C_3N	CH_3C_4H	CH_3C_5N	HC_9N	C_6H_6
AlF	C_2H	1-C_3H	C_4H	1-H_2C_4	CH_2CHCN	$HCOOCH_3$	CH_3CH_2CN	$(CH_3)_2CO$	C_7H_4	$HC_{11}N$
AlCl	C_2O	C_3N	C_4Si	C_2H_4	CH_3C_2H	CH_3COOH	$(CH_3)_2O$	$NH_2C_2H_3O_2$	$C_3H_6O_2$[1]	PAHs
C_2	C_2S	C_3O	1-C_3H_2	CH_3CN	CH_5N	C_7H	CH_3CH_2OH	$(CH_2OH)_2$		C_{60}
CH	CH_2	C_3S	c-C_3H_2	CH_3NC	$HCOCH_3$	H_2C_6	HC_7N			C_3H_8O
CH^+	HCN	C_2H_2	CH_2CN	CH_3OH	NH_2CH_3	$HOCH_2CHO$	C_8H			n-C_4H_7ON
CN	HCO	C_3H^-	CH_4	CH_3SH	c-C_2H_4O	1-HC_6H	$CH_3C(O)NH_2$			C_{70}
CO	HCO^+	HCCN	HC_3N	NC_3NH^+	C_6H^-	CH_2CHCHO	C_8H^-			
CO^+	HCS^+	$HCNH^+$	HC_2NC	NC_2CHO		CH_2CCHCN	C_3H_6			
CP	HOC^+	HNCO	HCOOH	NH_2CHO		H_2NCH_2CN				
CSi	H_2O	HNCS	H_2CHN	C_5N						
HCl	H_2S	$HOCO^+$	H_2C_2O	1-HC_4H						
KCl	HNC	H_2CO	HNC_3	1-HC_4N						
NH	HNO	H_2CN	SiH_4	c-H_2C_3O						
NO	MgCN	H_2CS	H_2COH^+	H_2CCNH						
NS	MgNC	H_3O^+	H_2NCN	C_5N^-						
NaCl	N_2H^+	NH_3	C_4H^-							
OH	N_2O	c-SiC_3	NC(O)CN							
PN	NaCH	CH_3								
SO	OCS	PH_3								
SO^+	c-SiC_2	HCNO								
SiN	CO_2	HOCN								
SiO	NH_2	HSCN								
SiS	H_3^+	H_2O_2								
CS	H_2D^+									
HF	SO_2									
HD	HD_2^+									
FeO	SiCN									
O_2	HCP									
CF^+	CCP									
SiH	AlOH									
PO	H_2O^+									
AlO	H_2Cl^+									
OH^+	KCN									
CN^-	FeCN									
SN^+										
CH										
CH^+										

Table 1.1: List of Molecules in the ISM (2011) (URL: Cologne Database for Molecular Spectroscopy (CDMS)).

In the clouds, there exist no inorganic molecules containing more than five atoms. Only the organic molecules can form bigger structures.
In my studies, I have analysed two inversion lines of ammonia. Ammonia (NH_3) has some advantages over carbon monoxide making it a practicable tool in star formation research. On the one hand, ammonia is a high-density tracer with critical densities in order 10^3 cm^{-3} (2083 cm^{-3} for (1,1)- and 1317 cm^{-3} for (2,2)-inversion transition). Thereby, it is helpful in finding clumpy structures within the ISM. On the other hand, the ammonia inversion lines are narrow and relatively near together in frequency space. Thus, one can observe two (or more) lines within one observation (contrary to carbonmonoxid).
The ammonia molecule itself contains one nitrogen atom and three hydrogen ones. They are arranged as an tetrahedron. The hydrogen atoms build the triangular basis and the nitrogen

[1] additional knowledge: Ethyl formate (C_2H_5OCHO) is an ester formed when ethanol reacts with formic acid. It has the characteristic smell of rum and is also partially responsible for the flavor of raspberries. (wikipedia.org).

atom the vertex. Thus, the molecule acts like a symmetric gyro with two principal axes of inertia. Therefore, it is able to rotate, as well as the individual atoms can vibrate against each other. But the molecule is no planar symmetric gyro, that is why it has also the property of inversion.

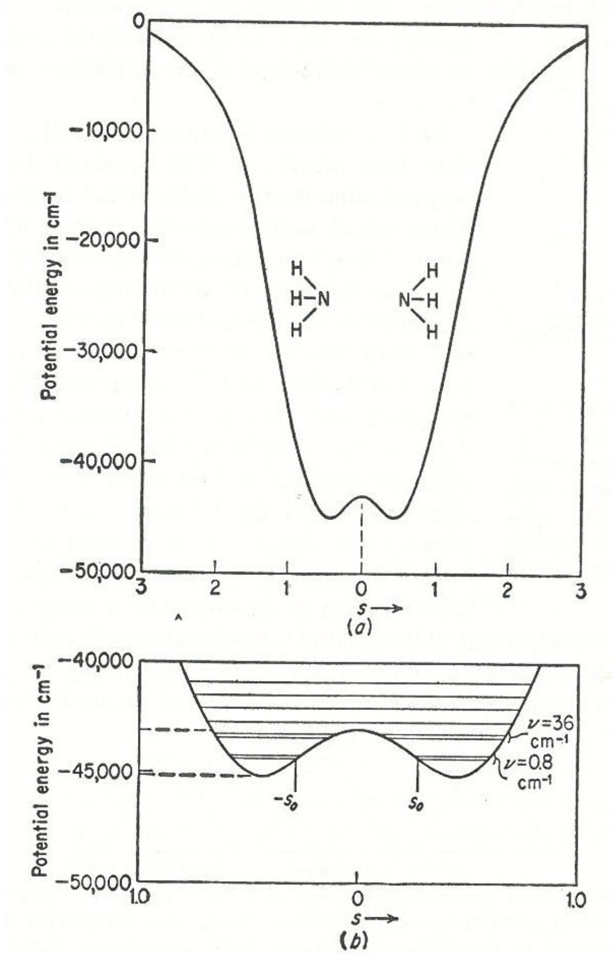

Figure 1.4: Potential curve of NH_3. s describes the distance between the nitrogen atom to the hydrogen plane. (b) is a magnification of the lower part of the potential curve, including the energy levels (Townes et al., 1975).

Fig. 1.4 shows a plot of the potential curve of NH_3 as a function of the distance between the nitrogen atom and the hydrogen plane. One can note that for lower energies there are two possible states of equilibrium: on the one hand the nitrogen atom being on the left side of the hydrogen plane, on the other hand being on the right side. These two stages are seperated by a finite high potential barrier. Thus, it is possible that the nitrogen atom tunnels through the barrier and oscillates between the different states of equilibrium (like an umbrella being frequently turned down, cf. fig. 1.5). This process is called *inversion*.
Theoretically, there should be no energy difference between these two states of equilibrium, in contrast to other quantum mechanical effects. But based on the Pauli exclusion principle, this

is not allowed, which leads to a small energy shift of ΔE. The frequency the nitrogen atom oscillates with is given by $\nu^{inv} = \frac{\Delta E}{h}$ (with h being the Planck constant). The energy difference ΔE depends also on other quantum numbers.

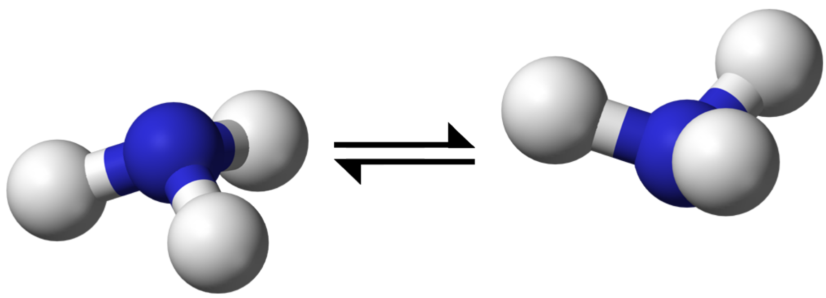

Figure 1.5: The Ammonia Molecule in the Two Possible States of Equilibrium (URL: Texas A&M Chemical Engineering Department).

For example, if one increases the molecule's angular momentum J, the distances between the individual atoms become bigger. That means, that the space between the hydrogen atoms becomes bigger. The consequence is that the potential barrier becomes smaller and the probability of the nitrogen tunneling through the plane increases. This effect is maximal, if the molecule's rotation is parallel to the symmetry axis (J = K). With smaller K (=J's projection on symmetry axis) the frequency decreases.
Simular to this, vibration causes an increasing inversion frequency, too. By vibration, the mean seperations between the individual atoms are bigger than in a state of rest, in particular the seperations between the hydrogen atoms.
But the inversion lines themselves are not enough to calculate the IRDCs' rotation temperatures and column densities. It is necessary to observe the lines' *hyperfine structures*.
The nitrogen nucleus is not spherically symmetric, that is why it has got a quadrupol moment. This interacts with the gradient of inhomogeneous electromagnetic field induced by the hydrogens' nuclei and electrons (Schilke, 1989). Thus, the nitrogen's nuclear spin $\mathbf{I}_N$ and the angular momentum of the molecule's rotation $\mathbf{J}$ link up to the temporary total angular momentum $\mathbf{F}_1$

$$\mathbf{F}_1 = \mathbf{I}_N + \mathbf{J} \tag{1.1}$$

Because the nitrogen's nuclear spin is $\mathrm{I}_N = 1$, F_1 can take the values

$$F_1 = |J-1|, J \text{ and } J+1 \tag{1.2}$$

Thus, one gets a hyperfine structure splitting for $\mathrm{J} \geq 1$ (cf. fig. 1.6) being the case in my studies. An example from the observed sample is shown in fig. 1.7.
There are also other interactions being explained in more details in Schilke (1989).

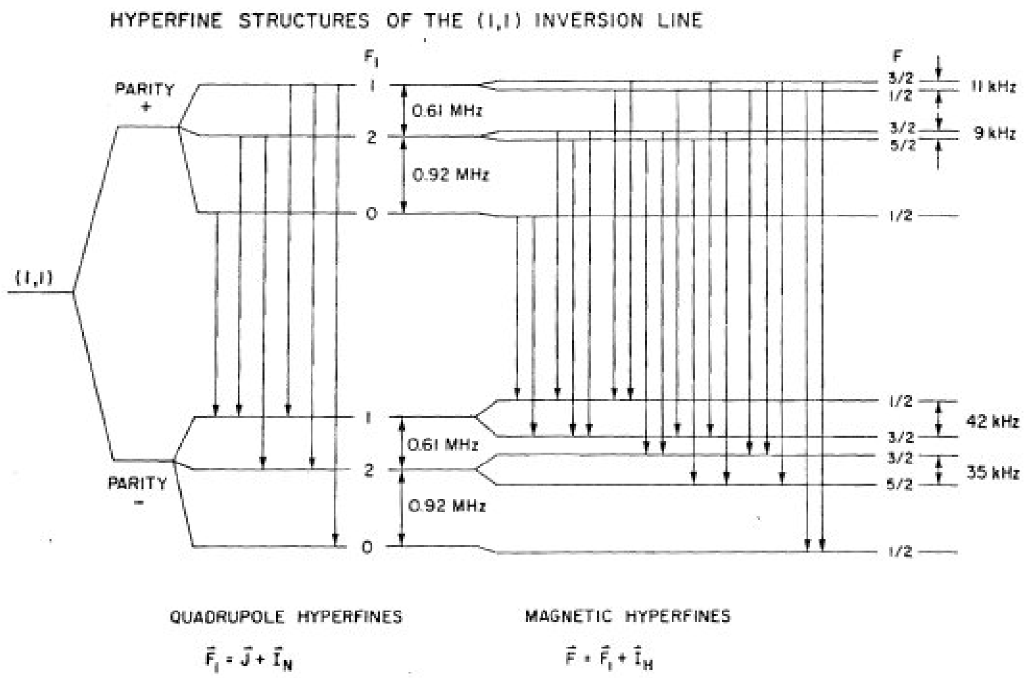

Figure 1.6: Hyperfine Splitting of the (J,K)=(1,1) Inversion Transition of Ammonia. The allowed transitions are indicated (Ho, 1977).

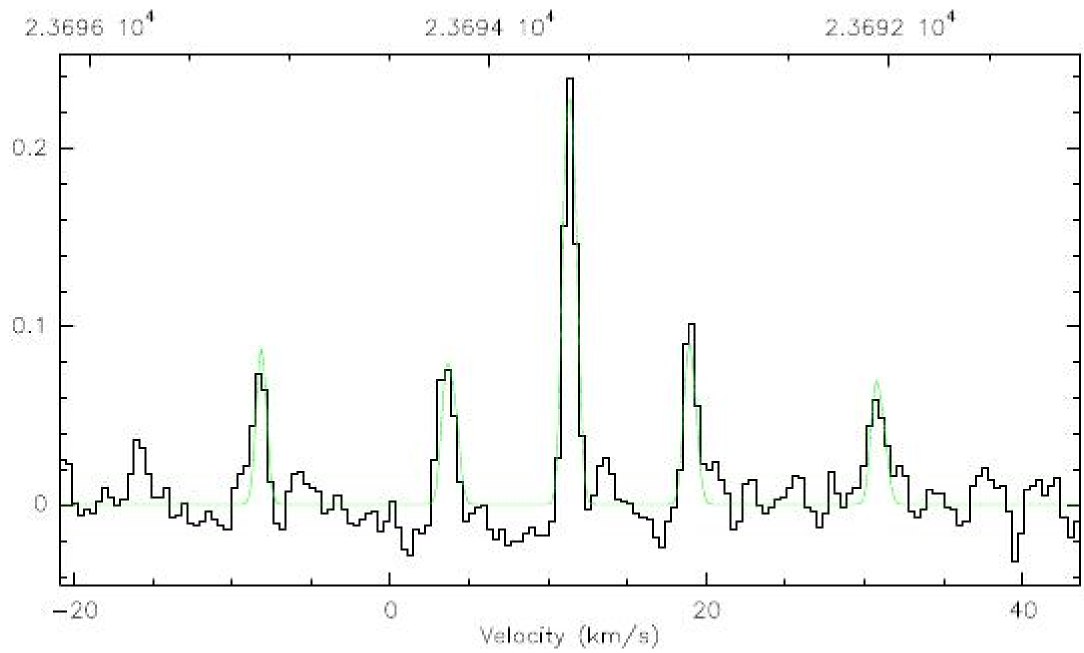

Figure 1.7: Observed Ammonia (1,1)-Inversion Line Hyperfine Structure in G34.34-00.72A

1.3 Radio Astronomy

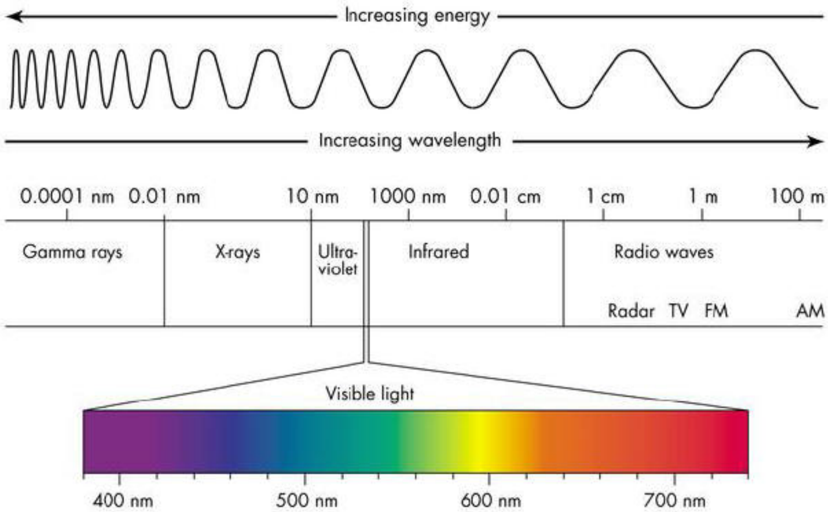

Figure 1.8: Spectrum of Electromagnetic Waves (URL: Antonine Education).

Fig. 1.8 shows the spectrum of electromagnetic waves and their classification. One can see that the part being visible for the human eye (400 - 750 nm) represents just a little fraction of this spectrum. Nevertheless, the beginning of astronomical observations started at these wavelengths. With the invention of the first telescope about 400 years ago, it was possible for astronomers to observe the sun and her planets more precisely. The inventions of photography and spectroscopy in the 19^{th} century allowed astronomers to look even deeper into the universe. This was seconded only by the start of manned and unmanned space flight allowing to overcome the limits of earth's atmosphere. But no matter, if one observes on earth or in orbit, the optical astronomy (the observation of sources in the range of visible light) does not suffice to explain the evolution and dynamics of stars, galaxies ect. As mentioned in ch. 1.1 the early stages of star formation are taking place in cold regions. Wien's displacement law

$$\lambda_{max} = \frac{2.898 \text{ mm K}}{\text{T}} \tag{1.3}$$

tells us that the wavelength of maximal radiation of a blackbody (as such we assume our sources) is inverse proportinal to its temperature. The colder the sources we want to observe, the bigger the wavelength at which we have to do that. Therefore, the beginning of radio astronomy was a great advance for star formation research.

The first to observe sources of radio waves from the Milky Way was Karl Jansky in the 1930s (Kraus, 1986). Jansky served in the field site of the Bell Telephone Laboratories as a radio engineer. His job was to study the effects of arriving thunderstorms on beam antennas of radio telescopes (which were used for transoceanic radio-telephone communication) and to find a way to increase the signal-to-noise ratio for the circuit. For this task, Jansky built the antenna which is seen in fig. 1.9. It was a vertically polarisated unidirectional beam antenna being about 30 m long, 4 m high and rotatable in azimuth.

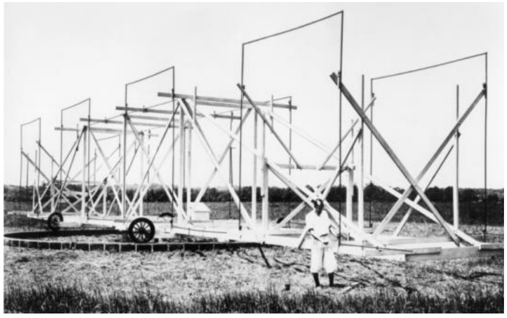

Figure 1.9: Karl G. Jansky and his Rotating Antenna Array

In December 1932, Jansky published his paper in the *Proceedings of the Institute of Radio Engineers* (Kraus, 1986) reporting his first results. He made out three groups of sources of disruption: firstly the local thunderstorms, secondly more distance thunderstorms (principally from southly directions), and thirdly "[...] a steady hiss type static of unknown origin" (Kraus, 1986). One year later, he presented his further studies saying that latter may "lead to the conclusion that the direction of arrival of these waves is fixed in space, i.e., that the waves come from some source outside the solar system" (Kraus, 1986). In 1935, Jansky published a third paper in which he came to the "conclusion that the source of these radiations is located in the stars themselves or in the interstellar matter distributed throughout the Milky Way" (Kraus, 1986). Further, he reasoned that if stars were sources, the sun itself should be a strong radiation source. This was not the case, because he did not observe any special radio radiation from the sun. Today we know that this is not exactly true and Jansky's observations took place during a sunspot minimum. Jansky also observed that the radio source followed an daily cycle of about 23 hours and 56 minutes. The strongest position of the radiation source has been located in direction of the centre of the galaxy. Jansky wanted to delve into the radio wave research, but was assigned to another project by his company. To honour his work and efforts, the unit of flux density, Jansky (Jy), was named by him.

The research in new radio astronomy was continued by others, like Grote Reber. In 1937, Reber built a parabolic-reflector antenna with a diameter of 9.5 m being steerable in declination and making use of the earth's rotation for moving in the right ascension (Kraus, 1986). After testing the limitations of his equipment and repeating Jansky's work, Reber started the first sky survey at radio wavelength (1.87 m or 160 MHz). The first maps were published in 1944 with a suprising good quality of measurements. Amongst others, Reber's publications piqued Prof. J. H. Oort's interest who suggested that the radiation Jansky and Reber detected has to be a continuum and that there could be also monochromatic lines in radio radiation. He tasked the astronomer Dr. H. van de Hulst to work out a possible mechanism for getting a line or single-frequency type of radiation in the radio spectrum. In 1945, van de Hulst also suggested that it would be worth to search for the 21.1 cm (1,42 MHz) line of neutral hydrogen. The line was detected in 1951 by Ewen and Purchell at Harvard University and Muller and Oort at Leiden. The observations of hydrogen and the surveys of the galaxy in this wavelength are of immense usefulness until today. But there were not only detections of radio radiation in our galaxy, but led also to the detection of radio galaxies.

There are different techniques to observe at radio wavelengths. But all contain an antenna collecting the radio radiation from the observed source and transfer the signal power to the main receiver. From there, the data are being recorded (cf. fig. 1.10). The data I have analysed in my studies were recorded by the 100 m radio telescope in Effelsberg.

The Effelsberg telescope is shown in fig. 1.11. It is a fully steerable parabolic single-dish antenna with a diameter of 100 m and a 40" FWHM at the NH_3 frequencies. Its construction has been finished in 1972 and it belongs to the Max-Planck Institute for Radio Astronomy (MPIfR) in Bonn since then. Until 2000, it was the world biggest telescope. More detailed informations about the techhnique of radio telescopes and the Effelsberg telescope can be found in the book of Kraus (1986) and the homepage of the Effelsberg Radio Telescope.

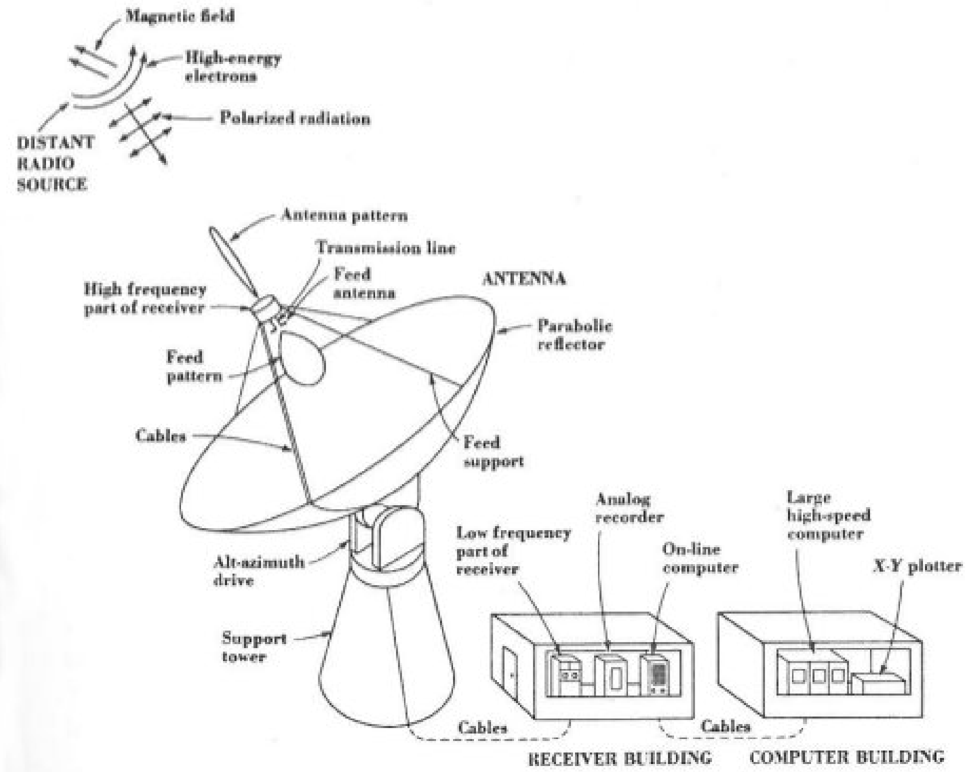

Figure 1.10: Schema of a Modern Radio Antenna (Kraus, 1986).

Figure 1.11: The 100m Radio Telescope in Effelsberg (URL: MPIfR).

1.4 The IRDC Sample

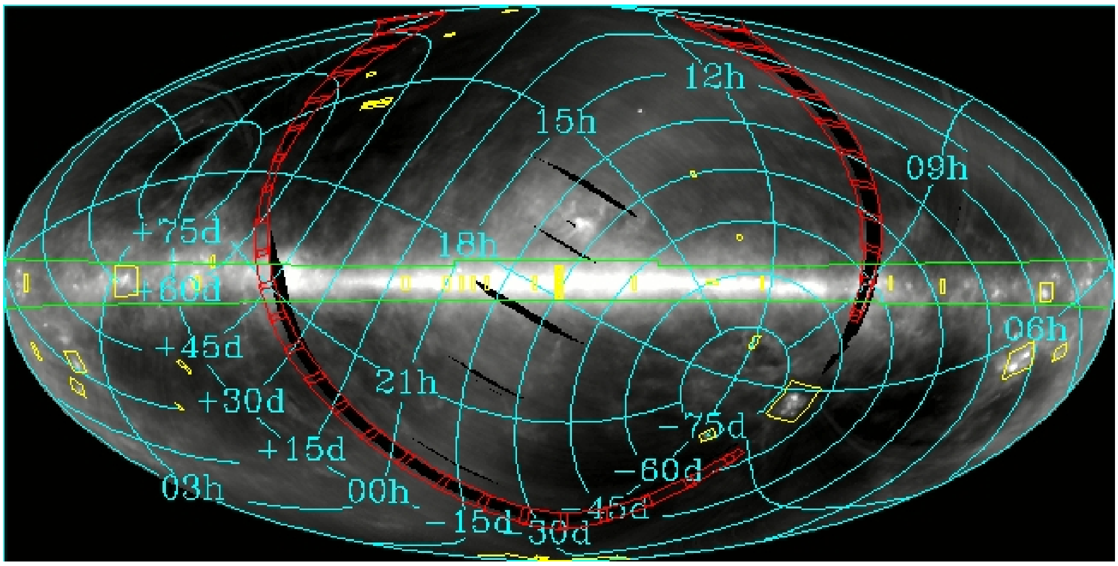

Figure 1.12: The Midcourse Space Experiment (MSX). In the background, an image of the Galactic Plane observed at 100 μm is shown. The blue grid indicates the J2000 Equatorial coordinates. The yellow regions represents the galaxies and star formation regions valiable also in higher resolution. The red regions show the IRAS Gap regions [2] (URL: R. Simon).

Based on the Midcourse Space Experiment (MSX), a catalogue of candidate IRDCs has been created, containing 10,931 candidate IRDCs and 12,774 embedded cores within the first and fourth quadrants of the Galactic plane (Simon et al., 2006). This area was surveyed by the MSX SPIRIT III, being launched in 1996, at the four mid-IR wavelength 8.3, 12.1, 12.7 and 21.3 μm (bands A, C, D, and E). The catalogue bases on the 8.3 μm data, because of its good combination of angular resolution and sensitivity.
The algorithm Simon et al. created for finding candidate IRDCs bases on the contrast being defined by contrast = (background - image) / background, and the requirement that IRDCs are isolated from each other, continuous, and extended. Thus, a candidate IRDC is detected, if the region's contrast is at least twice the error estimated for each pixel (to avoid detections by instrumental noise effects) and cover a larger area than $\Omega > \frac{\pi}{2} \cdot (28'')^2 = 1232$ arcsec^2 (IRDCs have to be extended). The candidate cores are found by two-dimensional elliptical Gaussian fits, so at least one core is found within each cloud. For more informations and details, please look at the paper of Simon et al. (2006).
For our observations we selected all candidate IRDCs being high-constrast (contrast value is higher than 0.3), extended (area is larger then 0.6 arcmin$^2 \approx 2160$ arcsec^2) and observable with the Effelsberg telescope (Galactic longitude l $> 20°$, Galactic latitude b $< 70°$). Also, the ratio of contrast to contrast error $c/\Delta c$ should be larger than 3 to obtain the clouds' significance. The 220 so selected candidate IRDCs were observed in 2008 and 2009 with the Effelsberg telescope in ammonia (1,1)- and (2,2)-inversion transitions.

[2] The Infrared Astronomical Satellite (IRAS) gap images were constructed from 160° long scans at constant ecliptic longitude (epoch 1984). Two sets of scans were performed covering the IRAS gaps at Ecliptic longitude ~162° (Gap 1) and ~342° (Gap 2) using 37 and 27 scans, respectively. The scans for each gap were offset by 0.45 degrees at the Ecliptic plane; therefore, scan coverage is a function of Ecliptic latitude with the highest sensitvities towards the Ecliptic poles (*MSX*).

1.5 The Atacama Pathfinder Experiment (APEX) Telescope Large Area Survey of the Galaxy (ATLASGAL)

One goal of my work should be to look for a way to classify IRDCs in comparision to high-mass protostellar objects (HMPOs). Therefore, the question whether the clumps are already collapsing or not is of great importance. But with the spectra of the Effelsberg telecope, it is only possible to calculate the virial masses (more details in ch. 2.4). To derive the gas mass I have used the dust continuum maps of the ATLASGAL Survey.
The APEX telescope large area survey of the galaxy (ATLASGAL) is a project exploring the Milky Way with the Atacama Pathfinder Experiment (APEX). The survey was done at submillimeter wavelengths in continuum (Schuller et al., 2009). It was concentrated on observations in the inner Galactic plane. The continuum emission of interstellar dust at 870 μm can be used for both locating high density regions (e.g. IRDCs) and deriving their masses, column densities and density structures and studying large-scale morphologies. Therefore, the survey was also used for building up a database of massive pre- and proto-stellar clumps in the Galaxy. There have been found about 6,000 compact source being brighter than 0.25 Jy (with a RMS of about 0.05 Jy), but only one third have an infrared counterpart. More details can be found in the paper of Schuller et al. (2009).
For deriving the masses of my sample of IRDCs, I needed to find the continuum counterparts of the IRDCs in the dust continuum maps and extract the flux densities (see ch. 2.4).

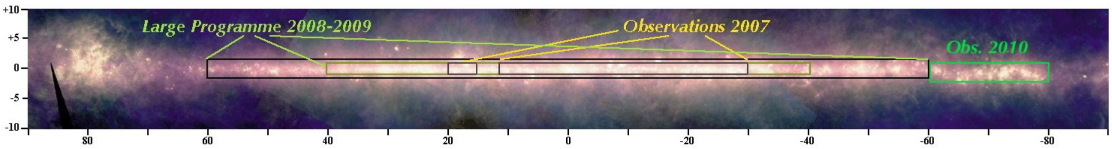

Figure 1.13: The APEX Telescope Large Area Survey of the Galaxy (ATLASGAL). In the background, the Galactic Plane is shown between ±90° in Gal. Longitude and ±10° in Gal. Latitude. Within that, the regions being observed by the ATLASGAL survey are indicated. From 2008 to 2010, the survey covered ±60° in Long., over ±1.5° in Lat., and again ±40° in Long., over ±1° in Lat., to improve the sensitivity in the innermost part of the Galactic plane. In 2010, another short project covered the regions between -80° to -60° in Long. and -2° to +1° in Lat., containing the last piece of activce star formation in the inner Galactic disk (Schuller et al., 2009).

2 Characterisation of Infrared Dark Clouds

The goals of my studies were to determine the initial conditions of 220 selected IRDCs by analysing their ammonia (1,1)- and (2,2)-inversion lines and find a way to classify them by comparing my results with the initial conditions of a high-mass protostellar object (HMPO) sample. In this chapter, I want to recapitulate the steps bringing me to my results.
In the end of my analysis, there were only 102 IRDCs with justifiable parameters left. The criteria for my selection were that

- the (1,1)-inversion line is detected,
- the relativ errors of their antenna temperatures is lower than 40%,
- the rotation temperatures are between 0 K and 50 K with (absolute) errors lower than 20 K and
- the counterpart regions of the IRDCs in the ATLASGAL dust maps have flux densities above the fourfold RMS.

Eight of the 220 observed sources have been detected in ammonia (1,1)-inversion transition, but have no counterparts in dust emission and have been sorted out. The following discussion will focus on this selection of 102 sources. The errors of the calcucated quantities have been computed by Gaussian error propagation. The presentation and interpretion of my results and the further characterisation will follow in chapter 3. In chapter 3.1 there will be a discussion about the other sources being sorted out.

2.1 Rotation Temperatures

For the calculations of the rotation temperatures and column densities, I have followed the desciptions of Schilke (1989, ch. 7.3) and Ho et al. (1983). For a better understanding, I will shortly summarise the most important points.
Effelsberg measured the IRDCs in two polarisations. Thus, there were two spectras for each clump needed to be averaged. This is possible, because the radiation of the sources is not polarized. The background noise has been reduced by frequency-switching. This mode changes the frequency of the system while still pointing at the same position. The so measured background radiation is substracted from the spectrum observed in the original frequency. This method has a great advantage over the position-switching. Here, one observed empty regions in the sky for about half the time for "just" measuring the background noise.
To average and frequency-switching the spectra and do the further analysis, I have used the GILDAS CLASS package (Hily-Blant et al., 2006) being created for analysing single-dish spectra of large quality. To derive the *velocity of observer relative to local standard of rest* (V_{lsr}), I needed to modify the spectra to the respective frequencies. That means that CLASS is able to calibrate the velocity values to a given frequency, so the V_{lsr} at this frequency is equal to zero.

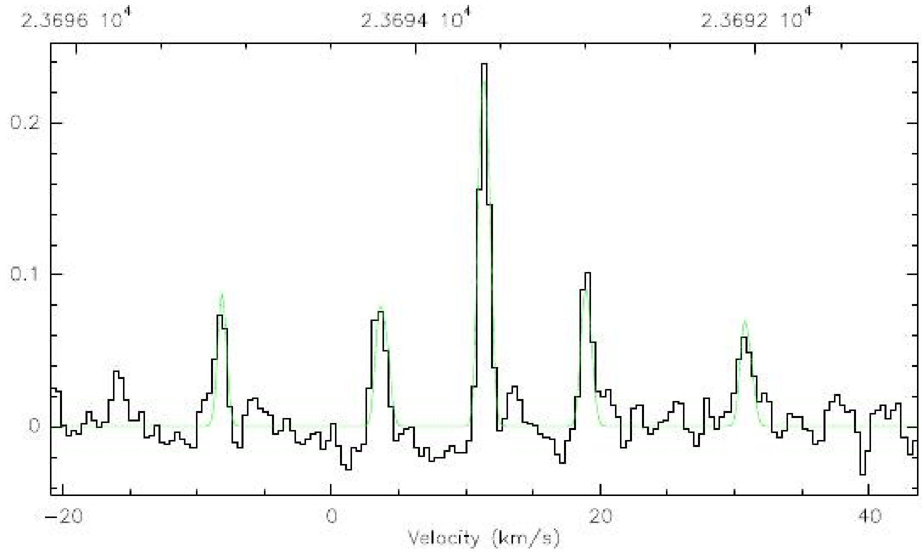

Figure 2.1: Observed Ammonia (1,1)-Inversion Line Hyperfine Structure in G34.34-00.72A

Because the sources are moving relative to us, the ammonia lines are shifted within the spectra. The derived V_{lsr} will help me to calculate the distances of the IRDCs from the sun (see ch. 2.3). After optimising the spectra by substrating polynomial baselines, I was able to fit the hyperfine structure of the inversion lines, assuming they were detected. The fit method for the ammonia inversion transitions is already included in CLASS. It bases on a multi-gaussian fit and needs the laboratory values for the frequency shifts and relative intensities of each hyperfine line, which can also be found in the thesis of Ho (1977). The hyperfine fit returns the best fit parameters for *antenna temperature* T_{ant}, *optical depth* τ, V_{lsr} and *linewidth* Δv (with errors). The important values for the detected ammonia inversion lines are listed up in table 1 in the appendix.
The *antenna temperature* T_{ant} describes the brightness temperature of a source. It depends on the beam with which the source is observed and returns the mean value over this beam. It is also needed to calculate the excitation temperature.
The *excitation temperature* T_{ex} is no physical quantities (because for masers it can also be negative), but descibes the ratio between two population levels u(p) and l(ow) via

$$\frac{n_u}{n_l} = \frac{g_u}{g_l} \exp\left(-\frac{\Delta E}{kT_{ex}}\right) \tag{2.1}$$

where n_i are the numbers of particle in the state i, g_i their statistic weights, ΔE is the energy difference between the states and k the Boltzmann constant. For the IRDCs it is expected to find temperatures above 10 K, wherefore the excitation and antenna temperatures are simplified (by the Rayleigh-Jeans law) by

$$T_{ant} = \eta_f (T_{ex} - T_{BG}) \cdot (1 - e^{-\tau}) \tag{2.2}$$

where τ is the optical depth and T_{BG} represents the background temperature being about 2.7 K.

For the excitation temperature, that means

$$T_{ex} = \frac{T_{ant}}{\eta_f(1 - e^{-\tau})} + 2.7\ \mathrm{K} \tag{2.3}$$

η_f represents the beam-filling factor describing the fraction of the antenna pattern being received from the source. In the case of extended and not lumped sources, the beam-filling factor is equal to 1. Because of a resolution of 40" (Effelsberg), this case can be assumed for the data. The excitation temperature can be calculated for both inversion lines with their respective optical depths.
But what we really want to know, is the *rotation temperature* T_{rot}. It is defined similiar to the excitation temperature by

$$\frac{n_i^l}{n_j^l} = \frac{g_i}{g_j} \exp\left(-\frac{\Delta E}{kT_{rot}^{ij}}\right) \tag{2.4}$$

But instead of the levels splitted by inversion, there are the levels of each quantum number J and K (total angular momentum and its absolute projection along the z-axis) needed. The index l represents the lower inversion level. Of interest are the rotation temperatures of the metastable inversion levels (J = K, for nonmetastable inversion levels J > K). Those levels cannot be destroyed by radiation. Therefore, the population numbers are high enough to emit measurable line intensities. Furthermore, they only interact via collisions. This will be very important for calculating the gas mass in ch. 2.4, because for temperatures below 50 K (expected for the IRDCs) the dust temperature is approximatly equal to the rotation temperature of ammonia (cf. Schilke, 1989).
The problem is that the population numbers are unknown and have to be approximated by the column densities. For lines detected in the same region the ratio of the population numbers should be equal to the ratio of the respective column densities. Latter depends on the ratio of the optical depths being described by

$$\begin{aligned} \frac{\tau^{JK}}{\tau^{J'K'}} &= \frac{K^2}{J(J+1)} \frac{J'(J'+1)}{K'^2} \frac{\Delta v_1}{\Delta v_2} \frac{N_l(J,K)}{N_l(J',K')} \frac{1 - e^{\frac{-h\nu_{JK}}{kT_{ex}^{JK}}}}{1 - e^{\frac{-h\nu_{J'K'}}{kT_{ex}^{J'K'}}}} \\ &\approx \frac{K^2}{J(J+1)} \frac{J'(J'+1)}{K'^2} \frac{2J'+1}{2J+1} \frac{\Delta v_1}{\Delta v_2} \frac{N_l(J,K)}{N_l(J',K')} \frac{\nu_{JK}}{\nu_{J'K'}} \frac{T_{ex}^{J'K'}}{T_{ex}^{JK}} \end{aligned} \tag{2.5}$$

where τ^{JK} is the optical depth of the (J,K) inversion line, Δv_i its linewidth, $N_l(J,K)$ its column density and T_{ex}^{JK} its excitation temperature. Because I am just analysing the (1,1)- and (2,2)-inversion lines, it is J = K = 2 and J' = K' = 1.

The excitation temperatures are expected to be much higher than the difference between the inversion levels (cf. Schilke, 1989). Therefore, the approximation in equ. (2.5) follows by the expansion of the exponential function. This can be solved for the ratio of the column densities and insert into equ. (2.4) getting:

$$T_{rot} = \frac{-E}{ln\left(\frac{K'^2}{J'(J'+1)} \frac{J(J+1)}{K^2} \frac{2J'+1}{2J+1} \frac{\Delta v_2}{\Delta v_1} \frac{\nu_{J'K'}}{\nu_{JK}} \frac{T_{ex}^{JK}}{T_{ex}^{J'K'}} \frac{\tau^{JK}}{\tau^{J'K'}}\right)} = \frac{-E}{ln\left(x \cdot \frac{\tau^{JK}}{\tau^{J'K'}}\right)} \tag{2.6}$$

where $E = \frac{h\nu_{ij}}{k} = 41.5$ K (Ho et al., 1983) and

$$x = \frac{K'^2}{J'(J'+1)} \frac{J(J+1)}{K^2} \frac{2J'+1}{2J+1} \frac{\Delta v_2}{\Delta v_1} \frac{\nu_{J'K'}}{\nu_{JK}} \frac{T_{ex}^{JK}}{T_{ex}^{J'K'}} \tag{2.7}$$

Following the instructions of Schilke (1989) and Ho et al. (1983), there are four cases for calculating the rotation temperature:

1. both inversion lines are optically thick:

$$T_{rot} = \frac{-E}{ln\left(x \frac{f_1}{f_2} \frac{\tau^{22}}{\tau^{11}}\right)} \tag{2.8}$$

   where τ^{ii} is the optical depth of the (i,i)-inversion line and f_i its average profile functions. There is $f_1 = 0.5$ and $f_2 = 0.796$ (Ho et al., 1983).

2. the (1,1)-inversion line is optically thick, but the (2,2)-inversion line is optically thin:

$$T_{rot} = \frac{-E}{ln\left(-x \frac{f_1}{\tau^{11} \cdot f_2} ln\left(1 - \frac{\tau^{22}}{\tau^{11}}(1 - e^{-\tau^{11}})\right)\right)} \tag{2.9}$$

3. both inversion lines are optically thin:

$$T_{rot} = \frac{-E}{ln\left(-x \frac{f_1}{f_2} \frac{T_{ant}^1}{T_{ant}^2}\right)} \tag{2.10}$$

   where T_{ant}^i is the antenna temperature of the (i,i)-inversion line.

4. the (1,1)-inversion line is detected, but not the (2,2)-inversion line (Ho et al., 1983):

$$T_{rot} = \frac{-E}{ln\left(-\frac{0.282}{\tau^{11}} ln\left(1 - \frac{T_{ant}^2}{T_{ant}^1}(1 - e^{-\tau^{11}})\right)\right)} \tag{2.11}$$

   In this case, the (2,2)-inversion line lies within the noise. T_{ant}^2 was given the spectrum's triple root-mean-square value (RMS = 0.025 K). Therefore, the rotation temperature derived with this case is just an upper limit estimation!

The results of these calculations can be for in table 2 in the Appendix and will be discussed in ch. 3.2 in more details. The sources' rotation temperatures are between 8 K and 29 K, with a mean value and median of about 15 K and errors of around 2 - 3 K.

2.2 Column Densities

The column densities of one inversion level (here: (J',K')) is related with the optical depth by (cf. equ. 2.5)

$$\begin{aligned}\tau^{J'K'} &= \frac{8\pi^3}{3h}\frac{2\sqrt{ln(2)}}{\sqrt{\pi}}\frac{K'^2}{J'(J'+1)}\mu^2\frac{1}{\Delta v_1}N_l(J',K')\cdot\left(1-\exp\left(-\frac{h\nu_{J'K'}}{kT_{ex}^{J'K'}}\right)\right)\\ &\approx \frac{8\pi^3}{3h}\frac{2\sqrt{ln(2)}}{\sqrt{\pi}}\frac{K'^2}{J'(J'+1)}\mu^2\frac{1}{\Delta v_1}N_l(J',K')\cdot\frac{h\nu_{J'K'}}{kT_{ex}^{J'K'}}\end{aligned} \tag{2.12}$$

where $\mu = 1.476{\cdot}10^{-18}$ Debye is the electric dipole moment. By neglecting the background radiation and expressing the excitation temperature in terms of the the optical depth, the column density of the (1,1)-inversion level can be calculated by

$$N_l^{11} = \frac{3.7}{1-e^{-\tau^{11}}}\frac{(\tau^{11})^2}{f_1}\frac{3h}{8\pi^3}\frac{\sqrt{\pi}}{2\sqrt{ln(2)}}\frac{J'(J'+1)}{K'^2}\frac{\Delta v_1}{\mu^2}\frac{k}{h\nu_1} \tag{2.13}$$

where ν_1 = 23694.496 MHz is the laboratory frequency of the (1,1)-inversion lines.
To get the total column density of the (1,1)-level, one needs to correct

$$N^{J'K'} = N_l^{J'K'}\cdot\left(1+\exp\left(-\frac{h\nu_1}{kT_{ex}^{J'K'}}\right)\right) \approx 2\cdot N_l^{J'K'} \tag{2.14}$$

But what we are interested in, is the total column density of all levels. Therefore, one has to assume that the clumps are in thermal equilibrium and the column densities follow the Boltzmann distribution

$$N^{J'K'} = \frac{N_{tot}}{Z}\cdot g_{J'K'}\cdot\exp\left(-\frac{h\nu_{J'K'}}{kT_{ex}^{J'K'}}\right) \tag{2.15}$$

with Z being the partition function

$$Z = \sum_{J,K} g_{JK}\exp\left(-\frac{h\nu_{JK}}{kT_{rot}}\right) \tag{2.16}$$

In addition, one has to consider that equ. (2.14) calculates only the column density of para-NH_3. Para-NH_3 descripes the ammonia inversion levels with K $\neq$ 3n (n being an integer) and not parallel hydrogen spins. In contrast, ortho-NH_3 unites all ammonia inversion levels with K = 3n and parallel hydrogen spins. The statistical weight g_{JK} of the two states is given by $g_{JK} = 2(2J+1)$ for para-NH_3 and $g_{JK} = 4(2J+1)$ for ortho-NH_3. That means, if one wants to calculate the total column density N_{tot} of ammonia, the left-hand side of equ. (2.15) has to be multiplied by a factor of three (because the abundance of ortho-NH_3 is twice the one of para-NH_3). In the end, the *total column density* of ammonia can be calculated by

$$N[\mathrm{NH_3}]_{tot} = \frac{3N^{J'K'}}{2(2J'+1)}Z\cdot e^{\frac{23.4}{T_{rot}}} \tag{2.17}$$

The results for the IRDCs are listed in table 2. The column densities range between $0.2{\cdot}10^{15}$ cm^{-2} and $38.7{\cdot}10^{15}$ cm^{-2}. The mean value of the column densities is approx. $6{\cdot}10^{15}$ cm^{-2} and the median about $4{\cdot}10^{15}$ cm^{-2}. These results will be discussed in more details in ch. 3.2, too.

2.3 Distances

To calculate the virial masses of the IRDCs in ch. 2.4, one needs their radii. Those can be estimated by calculating the distances of the IRDC from the sun and using the resolution of the Effelsberg telescope. The calculations of the IRDCs' distances to the sun were a little bit more complicated. At the end, I have just the algorithm of Reid et al. (2009) by translating their FORTRAN algorithm into C++ language and including it into my routine. The routine was originally thought for distance estimations by using maser lines. It uses their V_{lsr}, wherefore this method is also applicable for my ammonia lines. The kinematic distances are calculated by using the galaxy's rotation curve. The parameters of that rotation curve have been recalculated by Reid et al. Their best fits differ from the standard parameters of solar motion.
Therefore, in the first step, the routine converts V_{lsr} to a heliocentric frame by substracting the components of the standard solar motion. In the next step, the "new" V_{lsr} is computed by adding the best fit parameters of solar motion. Now, the angle between the sun, the IRDC and the GC and the IRDCs distance from the GC projected in the Galactic plane can be estimated. But one has to consider that for each V_{lsr} and position in the Galactic plane, there are two possible distances, in the majority of cases.
In this routine it is supposed that the galaxy has a flat rotation curve. That means that the rotation speed of the galaxy at the source is independed of its distance from the GC: $\frac{d\Theta}{dR} = 0$. Thus, the angular velocity is inversely proportional to the radius (distance of source to the GC). If one would measure the velocity in one direction, it would first increase, until the maximum is reached in the so called tangent point. Behind that the velocity curve would descrease again. Thus, for a given velocity there are two possible locations of the source: the one position before the tangent point, and the other one behind it. The IRDCs have been selected because of their high contrast against the Galactic background. Therefore, I am just interested in the nearer positions.
The error of the sources' distances is exstimated by repeating the upper routine and using the upper and lower error limits of V_{lsr}.
The sources of the sample are at distances of a few kilo-parsec (cf. table 2 in the Appendix). The positions of the sample IRDCs and HMPOs are sketched in fig. 2.2.

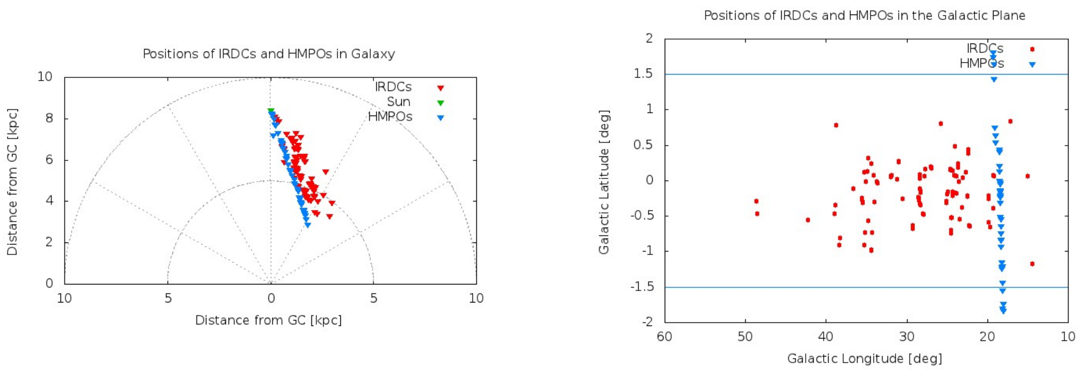

(a) Positions in Galaxy **(b)** Positions in Galactic Plane

Figure 2.2: Positions of selected IRDCs and HMPOs (cf. chapter 2) in the Galaxy

2.4 Virial And Gas Masses

2.4.1 Radii

The data received by the Effelsberg telescope have a FWHM of 40". Therefore, the angle is sufficiently small to estimate the radii of my IRDCs by trigonometry. For each source, the sun, the middle and the edge of the source build a right angle triangle (with the right angle between sun-middle-edge). The distance between the sun and the source's middle is given by the distance d calculated in ch. 2.3. The edge-sun-middle angle is given by half the FWHM of Effelsberg telescope (assuming the FWHM converts the whole source). Thus, the radius r is given by

$$\mathrm{r} = \mathrm{d} \cdot \tan\left(\frac{\mathrm{FWHM}}{2}\right) \tag{2.18}$$

The radii are between 0.25 pc and 0.5 pc (cf. table 2 in the Appendix).

2.4.2 Virial Masses

The *Virial Equilibrium* represents the state of an object being in equilibrium by balancing all acting fources, so that the sum of those is equal to zero. Because gravitational and kinematic energy are about the same order (but a factor of two), the easiest way to write down the Virial Equilibrium is

$$-\,\mathrm{W} = 2\mathrm{T} \tag{2.19}$$

where W represents the gravitational energy and T the kinematic one.
Solving equ. (2.19) for the mass and assuming a Gassian velocity distribution, the virial mass can be derived by

$$\mathrm{M} = k_2 \ \mathrm{r} \ \Delta v_1^2 \tag{2.20}$$

with r being the source's radius and Δv_1 the linewidth of the (1,1)-ammonia inversion line (MacLaren et al., 1988). The *Virial Mass* represents the mass a source needs to have for being in equilibrium with a given radius and linewidth (latter being an indicator for internal turbulences). If the gas mass (cf. ch. 2.4.3) is equal to the virial mass, the source should be in equilibrium. If the gas mass is greater than the virial mass, the source's self-gravity overbalances the internal turbulances and the clump is expected to collaps.
k_2 is a constant, but depends on the used density profile.

Density Distribution	k_2
$\rho = \mathrm{const}$	210
$\rho \sim \frac{1}{r}$	190
$\rho \sim \frac{1}{r^2}$	126

Table 2.1: Virial Theorem Coefficient (MacLaren et al., 1988)

It is not clear whether the sources' density profile follow a r^{-1}- or r^{-2}-law. Therefore, I have calculated the masses with equ. (2.20) for both density profiles. The virial masses presented in table 3 are the mean values of both profiles (the errors being the difference between the mean values and the profile masses).
The virial masses range between about 6 $M_\odot$ and 1100 $M_\odot$. The mean value is approx. 325 $M_\odot$

and the median around 264 $M_\odot$. The results and the correlation to the gas mass (ch. 2.4.3) will be discussed in ch. 3.3.

2.4.3 Gas Masses

For calculating the gas mass, I have used the dust emission maps of the ATLASGAL project (cf. Schuller et al., 2009, and ch. 1.5). Thus, the gas mass is given by

$$M = \frac{\mathrm{d}^2 \mathrm{F}_\nu R}{\mathrm{B}_\nu(T_D)\kappa_\nu} \tag{2.21}$$

(Schuller et al., 2009), where d is the source's distance to the sun, F_ν is the total flux density measured in dust emission at 870 μm. Therefore, the frequency ν is about 345 GHz. $\mathrm{B}_\nu(T_D)$ represents the Planck function for the dust temperature T_D

$$\mathrm{B}_\nu(T_D) = \frac{2h\nu^3}{c^2} \cdot \frac{1}{\exp\left(\frac{h\nu}{kT_D}\right) - 1} \tag{2.22}$$

where h is the Planck constant, k the Boltzmann constant and c the speed of light. The dust temperature T_D can be approximated by the rotation temperature of ammonia T_{rot} for temperatures below 50 K (Schilke, 1989). R represents the gas-to-dust mass ratio and κ_ν the dust absorption coefficient. Following the instructions of Schuller et al. (2009), R is assumed to be 100 and $\kappa_\nu = 1.85$ cm^2 g^{-1}. But these two quantities contain the biggest uncertainties, particularly the gas absorption coefficient. In the paper of Ossenkopf et al. (1994) its dependency on different initial distributions based on the models of Mathis et al. (1977) is described in detail. The gas absorption coefficient used in the ATLASGAL paper has been interpolated from Table 1, Col. 5 in Ossenkopf et al. (1994) at the wavelength of 870 μm. Interpolating the data of this column on my one, I have found a gas absorption coefficient of $\kappa_{OH} = (1.7 \pm 0.2)$ cm^2 g^{-1}. Though, the values differ slightly from each other, they are conformable with each other within the error range, as are the gas masses being calculated with them. Hence, I have only listed the gas masses with the ATLASGAL coefficient of $\kappa_\nu = 1.85$ in table 3.
I have also interpoled the gas absorption coefficient based on the original data of Mathis et al., given in Table 1, Col. 2 in Ossenkopf et al. (1994). This gave me a coefficient of $\kappa_{MRN} = (0.6 \pm 0.1)$ cm^2 g^{-1}. Since we do not know the exact value, this gives us a error approximation. Therefore, the uncertainty in κ_ν also implies an error factor of about 3 in gas mass (cf. table 3).
At last, I have had to extract the total flux densities from the dust maps. Because the 19.2" resolution of the ATLASGAL maps is much better than the 40" resolution of the Effelsberg data, there were two ways of doing this:

1. I use the original ATLASGAL data with the resolution of 19.2" and measure the flux within a cicle of the radius $\sqrt{\frac{1.133 \cdot (40\ \mathrm{arcsec})^2}{\pi}} \approx 24$ arcsec around the individual sources (fig. 2.3a).
   This area corresponds to one pixel at a resolution of 40". For this task, I have used the programme GILDAS GREG (Buisson et al., 2007). But, the routine cannot export the flux density within the circle area automatically. Therefore, I have had to trace the the circle line with a polygon. GREG calculates the integrated intensity within this polygon area. To get the flux density, I nedded to divide this by the area $1.133 \cdot (19.2\ \mathrm{arcsec})^2 \approx 418$ arcsec^2 representing the area of a Gaussian with a resolution of 19.2".

2. The second option is to smooth the original data to a resolution of 40" and measure the flux at the locations of the individual clumps (2.3b).
   The smoothing is done by GREG by folding the data with a Gaussian of 35.1" ($= \sqrt{40" - 19"}$) FWHM. Now, I could zoom into the smoothed maps and measure the flux density on the exact locations of my sources. But the smoothing affected only the resolution, not the flux data saved in the FITS-files. Therefore, the flux densities given out by GREG have to be corrected by the factor $\frac{40^2}{19.2^2} \approx 4.34$ representing the ratio of the Gaussian areas at resolutions of 40" and 19.2".

Both methods return approximately the same values of flux density. In my opinion, the first method is more defective than the second one, because the accuracy, the polygons were drawn with, differs from source to source. The second method just needs the data of one point being adjustable in a better way. Therefore, the gas masses being listed up in table 3 are calculated with the flux densities extracted with the second method. The relative error of flux density is assumed to be 20%. This is sufficient, because the masses' errors are dominated by the error of the dust absorption coefficient.

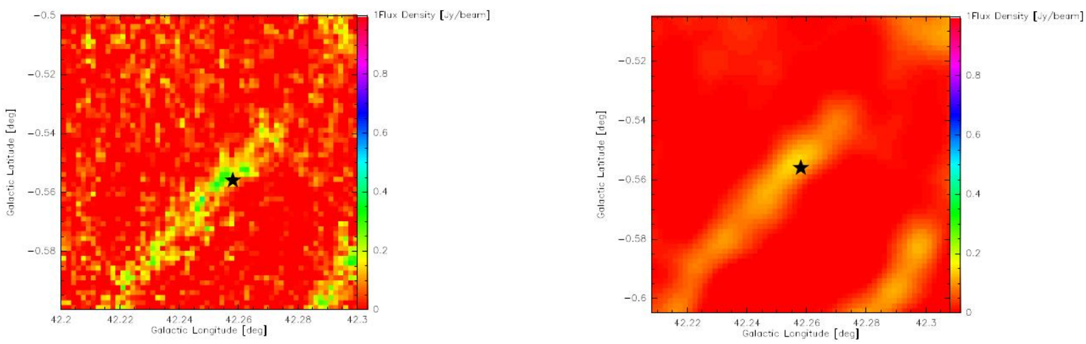

(a) Method 1: Deriving Flux Density via Integrated Intensity

(b) Method 2: Deriving Flux Density with Smoothed Maps

Figure 2.3: Deriving Flux Density. Example shown with G42.26-00.54A (Schuller et al., 2009)

3 Results and Interpretation

The process of star formation, both of low- and high-mass stars, takes place within a period between 10^5 and 10^7 years. This is too long for being fully observable within human lifetime. What we know about this process, is of statistical nature. Many star forming regions have already been observed. Within them, forming stars in different stages have been found. By bringing those stages in a physically justifiable order, the standard theory of star formation has been build up (cf. ch. 1.1). But for differentiating the stages of star formation, specific attributes within the initial conditions and observations have to be found. To characterise my sample of IRDCs, I have to compare their initial conditions with those of HMPOs.
High-Mass Protostellar Objects (HMPOs) are considered to be the next evolutionary step in high-mass star formation after the IRDCs. Because of the high opacity of the cloud embedding the early cores, the differentiation between these two stages cannot be done by observations only. Thus, the initial conditions of both have to be compared with each other. Therefore, I was given a sample of 65 HMPOs (Sridharan et al., 2002). The data are listed in table 4 in the appendix.
In this chapter, I will first explain, why sources were declared as "non-detected" and not further analysed. After that, I will discuss the initial conditions of the detected IRDCs derived with the formula presented in chapter 2 and compare them with those of the HMPOs.

3.1 Not Detected Sources

3.1.1 Not Detected in Ammonia Inversion Lines

As described at the beginning of chapter 2, I sorted the spectra according to their quality. Thus, there were only 102 sources of 220 (46%) with results being usable for the further analysis. The other 118 sources have been sorted out for various reasons.
Firstly, 33 sources had to be sorted out, because there were no ammonia (1,1)-inversion lines at all (fig. 3.1b). Since the (2,2)-inversion line being weaker than the (1,1)-inversion line, they have also not been detected. Thus, I have not been able to do any calculations for those sources. In addition to those, another 29 sources were found without detectable (2,2)-inversion lines, although the corresponding (1,1)-inversion lines have been observed. For this case, I was able to continue my calculations by using the instructions of Ho et al. (1983, cf. ch. 2.1). But the derived quantities are only upper limits and are, wherefore, seperately listed up in the tables 1 - 3 in the appendix.
Secondly, there were many spectras with (1,1)-inversion lines lying within the noise. Thus, the hyperfine fits by CLASS have been of no good quality; with particular big errors. For achiving a statistic with justifiable results, I have sorted out all spectra with relative antenna temperature errors bigger than 40%.

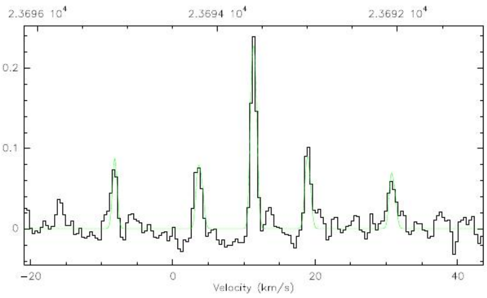

(a) Good Detected Ammonia (1,1)-Inversion Line G34.34-00.72A

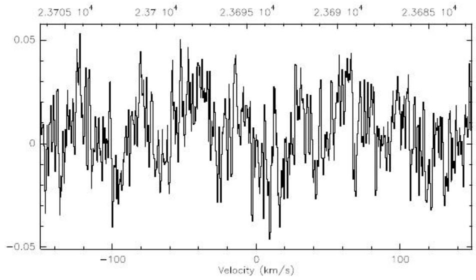

(b) Not Detected Ammonia (1,1)-Inversion Line G34.37-00.95E

Figure 3.1: Spectra of Detected and Not Detected Ammonia Inversion Transitions

3.1.2 Not Detected by ATLASGAL

For calculating the gas masses, I have had to find the IRDCs' counterparts in the dust emision maps of ATLASGAL. For obtaining the significance on these counterparts, I have claimed the flux densities of those counterparts to be higher than the fourfold of the maps RMS. It turned out that some IRDCs have no detectable counterparts in dust emission or ones lying within the noise. These eight sources have been sorted out, too.
Fig. 1 and fig. 2 in the appendix show the ATLASGAL emission maps in the range between 12° and 51° in Gal. Longitude. The sample IRDCs' positions are indicated by red triangles.

3.1.3 Distribution within the Galactic Plane

In fig. 2.2b, one can see that the IRDC are located close to the Galactic mid-plane (Gal. Latitude $b \sim 0°$). This makes sense, if one compares that with Fig. 5 of Schuller et al. (2009). These histograms show the distribution of the about 6,000 compact sources detected by ATLASGAL in Galactic Longitude and Latitude. Though, the distribution in Galactic Longitude is not uniform, the distribution in Galactic Latitude clearly is with a peak around the Galactic plane. Therefore, observations within the range of $|b| \leq 0.5°$ are recommended for building up a statistic of IRDCs. This can also be certified by the sample.
Because the compact sources are uniformly distributed in Gal. Latitude b (Schuller et al., 2009), I have ploted the distributions of the detected and not-detected sources in absolute Gal. Latitude $|b|$ in fig. 3.2. Both the mean value and median of the positions of the detected sources (mean: 0.307°, median: 0.227°s) are smaller than these of the not-detected sources (mean: 0.458°, median: 0.347°). This can be considered as additional evidence that IRDCs - and in general high-mass star-formating regions - are found close to the Galactic mid-plane.

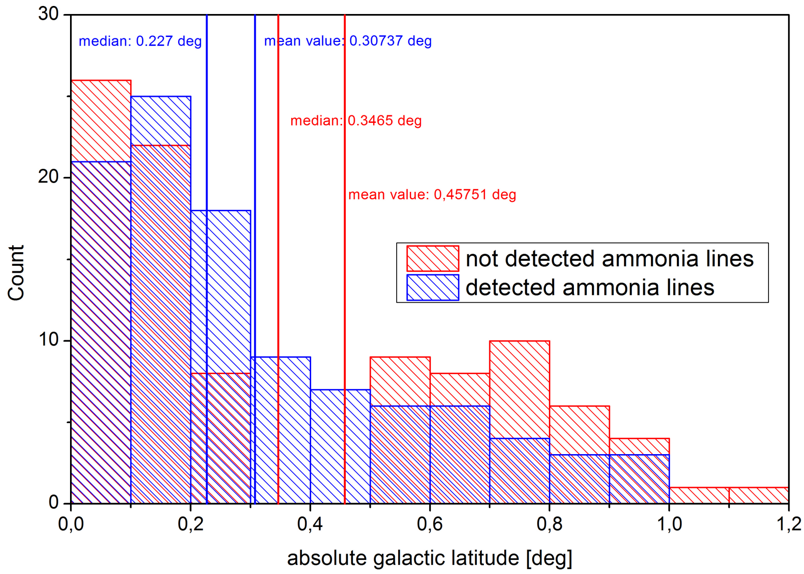

Figure 3.2: Distribution of Detected and Not-Detected sources in absolute Galactic Latitude. The mean values and medians of each distributions have been marked.

3.2 Conditions within IRDCs and HMPOs and Comparision

In table 3.1, a short statistic of the initial conditions of my IRDCs and the sample HMPOs is listed with the mean, minimal, maximal values, and median of the important quantities.
The IRDCs are at distances of a few kilo-parsec and have radii in order of 0.5 pc.
The rotation temperatures are between 8 K and 29 K. Although latter being a high limit, the majority of the IRDCs' have rotation temperatures around 15 K (both mean and median). The HMPOs are, with rotation temperatures about 25 K (∼22 K, Beuther et al., 2007), statistically warmer than the IRDCs (mean: 26 K, median: 24 K). The cumulative distribution function[3] in fig. 3.4a shows that clearly. The distribution representing the IRDCs starts earlier than the one of the HMPOs and increases much faster. The IRDC distribution reaches the maximum value earlier than the HMPO one, too. That means, that the IRDCs are signifantly colder than the HMPOs. Thus, it is possible to state that the rotation temperature increases with the clouds' evolution. Therefore, it is a good parameter for differentiating and characterising both stages.
Such comparision can also be done for the linewidth (fig. 3.4b and fig. 3.3b). The mean values and medians are higher for HMPOs (mean: 2.1 km s^{-1}, median: 2.0 km s^{-1}) than for IRDCs (mean & median: 1.7 km s^{-1}). Also, the cumulative distribution function of the HMPOs is significantly shifted to higher linewidths in comparision to the IRDCs' one (fig. 3.4b). This makes sense, because the linewidth is an indicator for turbulent motions within the sources, like the feedback of outflows.
In contrast, the column densities of both IRDCs (mean: $5.9{\cdot}10^{15}$ cm^{-2}, median: $4.1{\cdot}10^{15}$ cm^{-2}) and HMPOs (mean: $4.2{\cdot}10^{15}$ cm^{-2}, median: $2.6{\cdot}10^{15}$ cm^{-2}) are about the same order (fig. 3.4c

[3] The distribution function, also called the cumulative distribution function (CDF) or cumulative frequency function, describes the probability that a variate x takes on a value less than or equal to a number x (URL: WolframMathWorld).

and fig. 3.3b), as are the statistic values in table 3.1 and the cumulative distribution functions in fig. 3.4c. This can be interpreted as evidence that in this part of star formation the column density, and thus the abundance, of ammonia is not changing. Therefore, the column density cannot be used for classifying IRDCs.
In summary, while column densities stay approximately constant through the early evolutionary phases, we identify clear evolutionary trends in the rotation temperature and linewidth distributions. As soon as a central star forms, the gas clumps heat up and turbulent motions rise.

	mean value	minimal value	median	maximal value
IRDCs	number of sources = 102			
Rotation Temperature T_{rot} [K]	15 ± 1	8	15	29
Col. Density N[NH_3] [10^{15} cm^{-2}]	5.9 ± 0.6	0.2	4.1	38.7
Line Width Δv [km s^{-1}]	1.7 ± 0.1	0.7	1.7	4.0
Distance d [kpc]	3.3 ± 0.1	0.4	3.2	5.8
HMPOs	number of sources = 65			
Rotation Temperature T_{rot} [K]	26 ± 1	16	24	56
Col. Density N[NH_3] [10^{15} cm^{-2}]	4.2 ± 0.5	0.3	2.6	21.0
Line Width Δv [km s^{-1}]	2.1 ± 0.1	1.1	2.0	4.0

Table 3.1: Statistics of Conditions within IRDCs and HMPOs

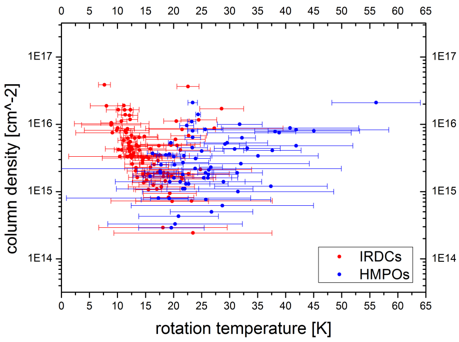

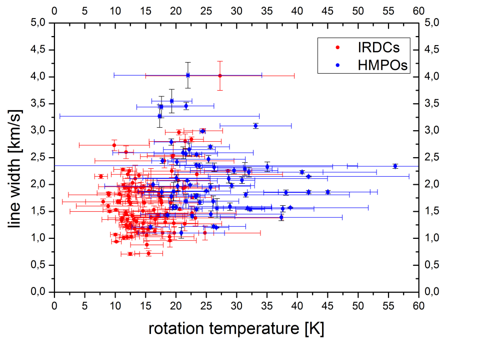

(a) Column Density against Rotation Temperature

(b) Line Width against Rotation Temperature

Figure 3.3: Comparision of IRDCs and HMPOs

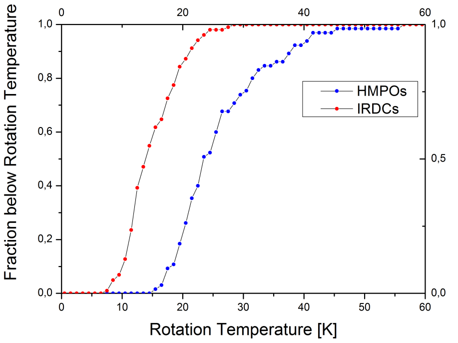

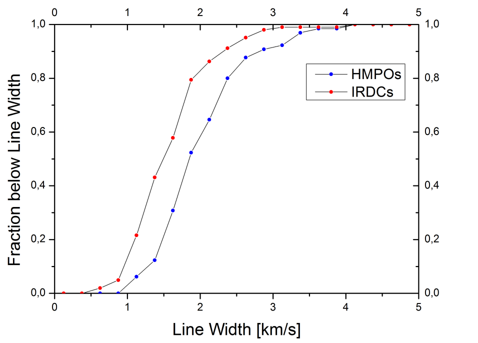

(a) Rotation Temperature

(b) Line Width

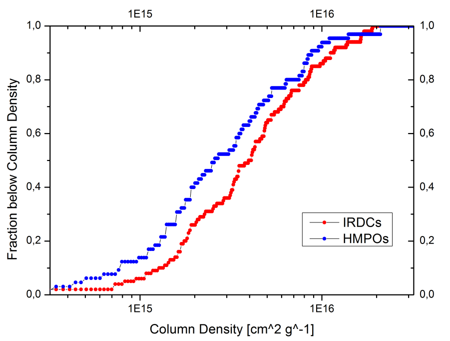

(c) Column Density

Figure 3.4: Cumulative Distribution of NH_3 (1,1)-Inversion Line Data

3.3 Virial Parameter

The virial masses of the IRDCs are in order between 100 and a few 1000 $M_\odot$ (cf. table 3.2 and table 3).

	mean value	minimal value	median	maximal value
IRDCs	number of sources = 102			
Virial Mass M_{vir} [$M_\odot$]	325 ± 25	6	264	1099
α_{gas}	6.1 ± 1.7	0.3	2.3	155.2
α_{MRN}	1.9 ± 0.5	0.1	0.7	49.4

Table 3.2: Statistics of Virial Mass and Virial Parameters of IRDCs

Following the defintion of Bertoldi et al. (1992), the *virial parameter* for molecular clouds is defined by

$$\alpha = a \cdot \frac{2T}{|W|} = \frac{M_{vir}}{M_{gas}} \tag{3.1}$$

where the dimensionless parameter a represents the correction factor for sources having no uniform and spherical mass distribution. T and W are the kinetic and gravitational energies (cf. equ. (2.19)). The ratio of kinetic and gravitational energy is equivalent to the ratio of virial (representing kinetic energy) and gas mass (representing gravitational energy). The virial parameter is a helpful tool, because it is an indicator for sources being in virial equilibrium or not. In a simplified picture, if one source's virial parameter is equal to 1, the source is in virial equilibrium, because the kinetic energy is able to balance gravitational energy. If the virial parameter is much greater than 1, turbulences are more powerful than the source's self-gravity and the source expands. In contrast, for a virial parameter much smaller than 1, self-gravity overbalances its counterpart and the source collaps.

In reality, there are additional effects like gas pressure, external pressure and magnetic fields influencing a cloud's state of equilibrium. Even clouds with $\alpha \gg 1$ are able to be in virial equilibrium.

The two plots in figure 3.5 show the virial masses, I have derived for the sample IRDCs, ploted against their corresponding gas masses. In fig. 3.5a, this is done for the gas mass calculated for the gas absorption coefficient of Ossenkopf et al. (OH model, 1994, Table 1, Col. 5); in fig. 3.5b for the gas absorption coefficient of Mathis et al. (MRN model, Ossenkopf et al., 1994, Table 1, Col. 2). The straight lines indicated in the plots represents the region of $\alpha = 1$.

For the OH model the majority of the sample IRDCs' virial parameters α_{gas} are in order of 1 (mean value: 6.1 ± 1.7, median: 2.3, cf. table 3.2). In contrast, the majority of the IRDCs' virial parameters α_{MRN} are shifted to smaller values for the MRN model (mean value: 1.9 ± 0.5, median: 0.7, cf. table 3.2). The discrepance between both plots is caused by the different gas absorption coefficient implying an error factor of about 3. Because it is not known which model satifies reality better, the models can be interpreted as upper and lower limits of the real virial parameters which should be approx. 1. But as mentioned before, this does not automatically imply that the sources are in equilibrium, because other terms influence the balance.

In my calculations, I have assumed that the sources' equilibrium depends only on the balance between kinetic and gravitational energy (cf. equ. (2.19)). Other parameters like pressure terms, magnetic fields and boundary conditions have been ignored, though they are able to shift the balance of forces in either direction. For example, close-by supernova explosions or young stars

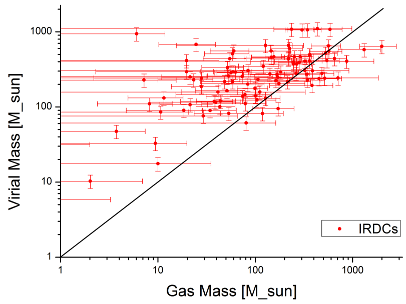

(a) Model of Ossenkopf et al. (1994): $\kappa = 1.85$ cm^2 g^{-1}

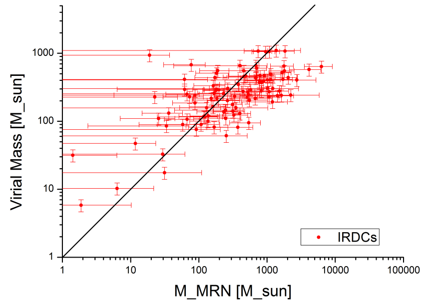

(b) Model of Mathis et al. (1977): $\kappa = (0.6 \pm 0.1)$ cm^2 g^{-1}

Figure 3.5: Virial Parameter in Dependency of the Gas Absorption Coefficient

can increase the average gas velocity and thus the linewidth. Therefore, the ignored quantities imply an additional error factor to the calculated virial mass. A more detailed discussion of underestimates and possible error sources by a simplified virial theorem is descriped in the paper of MacLaren et al. (1988).
Additionally, there is a big uncertainty in the present density profile. As described in ch. 2.4.2, the first step in deriving the IRDCs' virial masses has been to calculate the masses for two different density profile ($\sim r^{-1}$ and $\sim r^{-2}$). The mean value of those masses has been defined to be the resulting virial mass (cf. table 3, appendix). But this method implyies that there is no tendency to either profile, which is not known. It could be possible that the sources' density profiles tend towards one of these profiles, thus that profile has to be weighted more than the other one.
To sum up, that means that there are a lot of problems which need to be solve by better observations and theoretical models for reducing the uncertainty of my results. But in the bounds of my possibilities, I can say that the majority of the observed IRDCs are in virial equilibrium.

4 Summary and Conclusion

220 sources have been observed in (1,1)- and (2,2)-ammonia inversion transition lines being located between 10° and 50° in Galactic longitude and ±1.5° in Galactic latitude by the 100 m-Effelsberg radio telescope. In 102 sources, ammonia inversion lines have been detected. This sample allows me to build up a statistic of IRDCs' initial conditions. The majority of IRDCs have linewidths between 0.5 and 2.5 km s^{-1}, but some range up to 4 km s^{-1}. These linewidths are much higher than it would be expected from thermal NH_3 linewidths being about 0.1 km s^{-1} [4]. Thus, the derived linewidths are indicators for the turbulences within the clumps. They are smaller than the HMPOs' linewidths, but also higher than the linewidths in low-mass cores (Jijina et al., 1999). That could be interpreted as an evidence for the formation process of high-mass stars being similar to that of low-mass stars, but with increased parameters. The rotation temperatures are between 7 and 30 K, but on average at 15 K and, thus, cooler than HMPOs ($\sim$ 22 K). The column densities of both IRDCs and HMPOs do not differ from each other in a significant way. Hence, it is supposed that the abundance of ammonia does not change in these early stages of high-mass star formation.
The IRDCs' virial masses are between 100 and a few 1000 M$\odot$ and their virial parameters averaged in order of 1. Thus, it is assumed that the majority of clumps are in virial equilibrium.

My work helped me to learn more about the techniques of astrophysical observations and their limitations. It was suprising how much one can derive about a source's initial conditions with just one spetrum. Even for the sources with just the ammonia (1,1)-inversion line being detected, upper limits for rotation temperatures and column densities could be estimated. I have been also suprised about little information we actually have about these early stages of high-mass star-formation. There have been only smaller samples observing in ammonia transition, each containing only about 10 or 20 sources (e.g. Pillai et al., 2006; Sridharan et al., 2005). Therefore, it is needed to collect more information of high-mass star-forming regions by observing more of such sources.
But what I have been worried about, are the big errors of the calculated quantities (cf. table 1 - 3 in the appendix). This results from the limitations of the used technique. The figures in fig. 2.3 demonstrate that in a good way. Fig. 2.3b illustrates how the Effelberg radio telescope "sees" the universe with a FWHM of 40" at ammonia transitions. The source is, of course, identifiable, but the shape is blurred and it is difficult to define clear structures. In comparison to this, fig. 2.3a shows a much more detailed topology by "just" using a telescope with a smaller FWHM (APEX: 19.2"). Here, it is possible to differentiate smaller and finer clumps from each other in regions appearing uniform in the smoothed map. I am sure that the errors of my data could be reduced by using a telescope with a better resolution. An increased signal-to-noise ratio would also help by reducing the RMS observed spectra noise. Thus, the hyperfine structures of, inter alia, the ammonia inversion lines can be better detected and analysed. That would not only cause that more lines are detected (in my sample, only 46% of all observated spectra have got detectable (1,1)-inversion lines), but also that the errors of the quantities derived by the fitting

[4] For a clump with a temperature of $T = 15$ K and a molare mass of ammonia $m_{mol} = 17.03$ g mol^{-1}, the thermal linewidth can be calculated via $\Delta \mathrm{v} = \sqrt{3\ ln(2)\ \frac{kT}{m_{mol}})} \approx 0.12$ km s^{-1}

process decrease.
For future observations, there are some considerations being able to increase the detection rate, too. On the one hand, the selection of sources going to be observed could base on the ATLASGAL catalogue instead of the catalogue based on the MSX data. The chances are that almost all sources with high flux densities have got counterparts in the MSX catalogue (cf. Schuller et al., 2009, Fig. 12). On the other hand, the observations could be focused on an area of small Galactic latitudes ($|b| \lesssim 0.5°$). The majority of compact sources detected by ATLASGAL can be found here (Schuller et al., 2009, Fig. 5; ch. 3.1.3). Thus, the probability of detecting IRDCs in ammonia transition in this area is higher than in outer regions.

Appendix

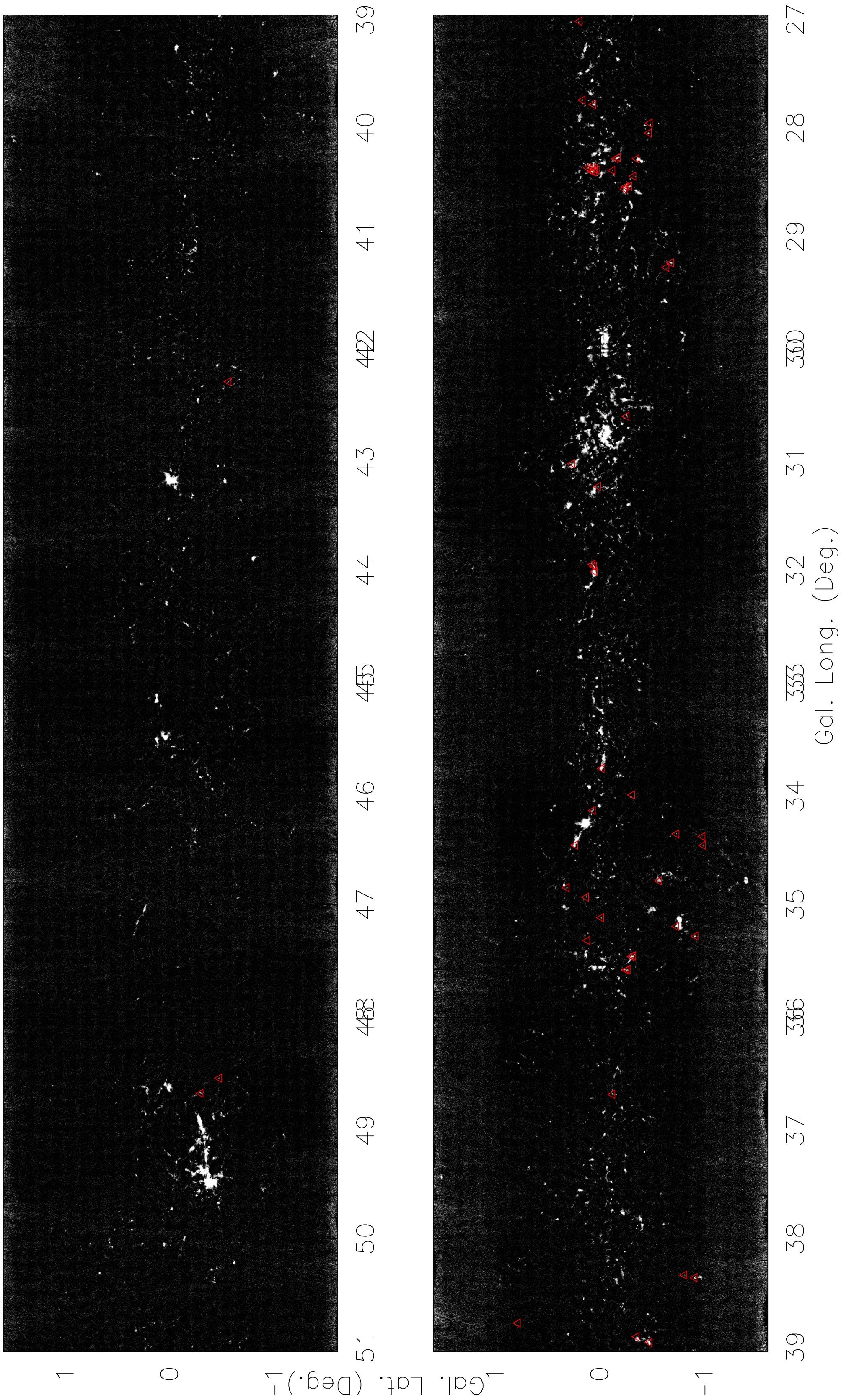

Figure 1: ATLASGAL Dust Emission Map with Indicated Sample IRDCs in the Range of l = 27° to 51° (Schuller et al., 2009).

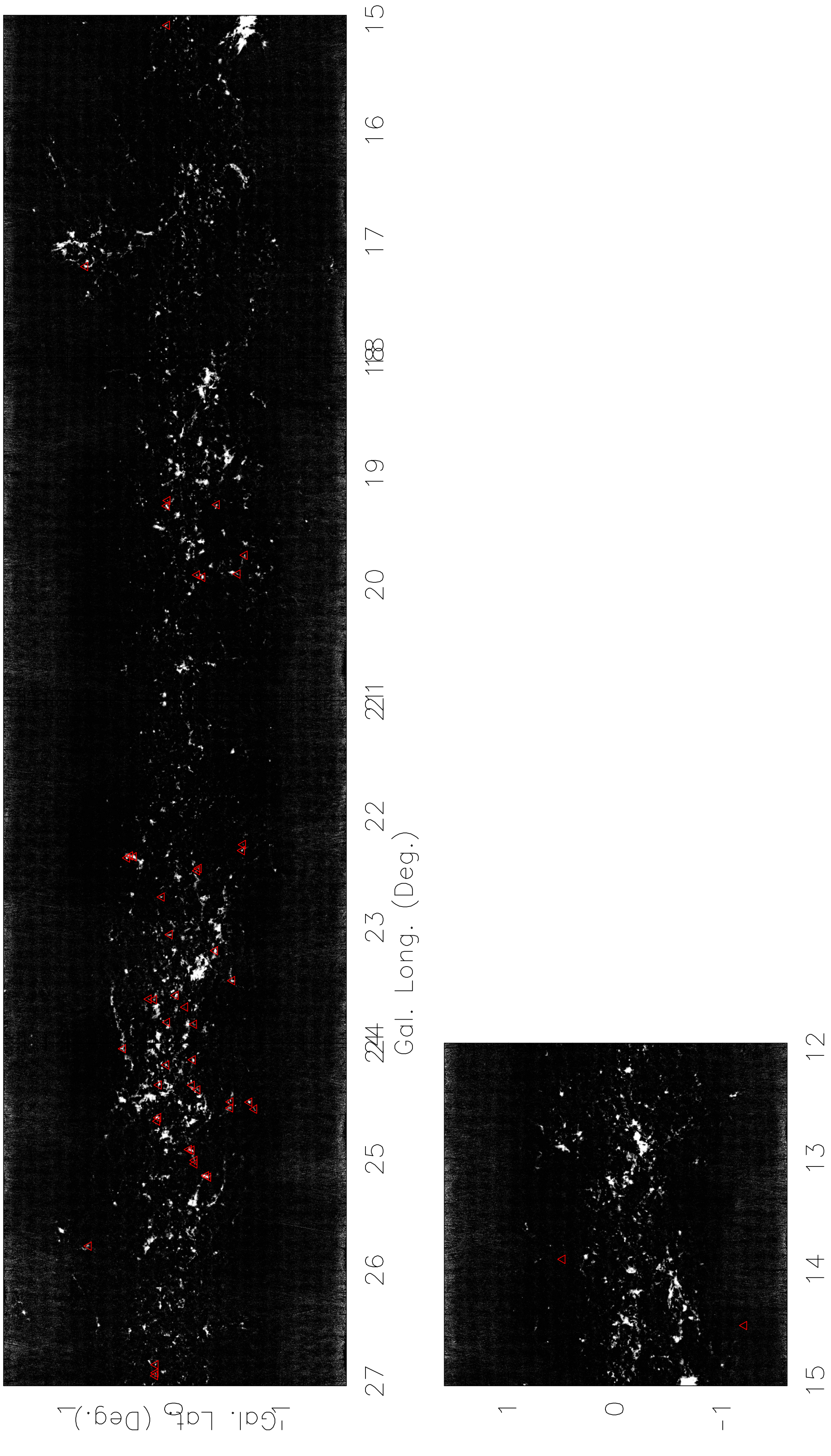

Figure 2: ATLASGAL Dust Emission Map with Indicated Sample IRDCs in the Range of l = 12° to 27° (Schuller et al., 2009).

Table 1: Coordinates and Fit Parameters of detected IRDCs in NH_3

Source	Gal. Long.	Gal. Lat.	T^1_{ant}	±	$v_{LSR,1}$	±	Δv^1	±	τ^{11}	±	τ^{22}	±
	deg		K			km s^{-1}						
G15.05+00.07A	15.048	0.071	0.380	0.070	29.900	0.017	1.020	0.041	2.660	0.290	10.210	4.500
G17.33+00.88A	17.218	0.836	0.490	0.031	22.540	0.013	1.680	0.031	1.360	0.110	0.100	0.350
G19.27+00.07A	19.289	0.076	0.680	0.041	26.900	0.012	1.840	0.025	2.240	0.100	0.100	0.096
G19.27+00.07B	19.241	0.068	0.090	0.031	25.770	0.140	4.020	0.270	1.840	0.570	4.030	1.600
G19.27-00.39A	19.279	-0.391	0.310	0.056	53.530	0.027	1.110	0.071	1.210	0.340	3.410	1.400
G19.73-00.66A	19.733	-0.652	0.400	0.046	23.570	0.021	1.310	0.052	1.180	0.210	2.040	1.400
G19.91-00.20A	19.911	-0.207	0.120	0.042	63.550	0.100	2.080	0.190	2.190	0.620	1.750	1.700
G19.91-00.20A	19.911	-0.207	0.120	0.033	63.510	0.063	1.930	0.150	1.840	0.450	1.750	1.700
G19.92-00.29A	19.931	-0.257	0.700	0.065	65.240	0.026	2.970	0.048	2.550	0.150	1.250	0.290
G19.92-00.29A	19.931	-0.257	0.520	0.040	65.350	0.023	3.000	0.041	2.600	0.130	1.250	0.290
G22.24-00.63A	22.254	-0.637	0.190	0.040	47.990	0.048	1.660	0.110	1.290	0.380	1.860	2.800
G22.35+00.41B	22.356	0.416	0.200	0.033	84.040	0.062	2.190	0.180	0.190	0.330	0.100	0.390
G22.35+00.41A	22.374	0.444	0.310	0.047	52.660	0.038	1.950	0.088	1.470	0.270	3.890	1.800
G22.56-00.20F	22.469	-0.222	0.390	0.058	75.830	0.023	1.180	0.060	1.450	0.260	0.660	1.800
G22.73+00.11A	22.726	0.123	0.240	0.052	78.000	0.054	1.880	0.140	1.510	0.380	2.990	1.900
G23.06+00.04A	23.064	0.046	0.210	0.049	91.320	0.036	1.660	0.075	2.500	0.370	2.900	1.900
G23.22-00.37A	23.209	-0.376	0.830	0.067	77.660	0.012	2.250	0.024	3.690	0.120	1.590	0.320
G23.42-00.52A	23.478	-0.537	0.280	0.064	64.180	0.029	1.880	0.053	3.580	0.350	2.710	1.600
G23.60+00.00A	23.611	-0.009	0.550	0.078	53.640	0.021	1.680	0.043	2.850	0.220	2.860	1.000
G23.71+00.30A	23.644	0.243	0.270	0.079	110.900	0.040	1.190	0.100	1.770	0.480	5.090	3.500
G23.71+00.30B	23.648	0.193	0.230	0.070	87.780	0.057	1.400	0.180	0.920	0.560	7.200	3.400
G23.87+00.07A	23.853	0.071	0.260	0.040	54.150	0.016	1.110	0.037	2.520	0.240	0.720	1.300
G23.86-00.19A	23.871	-0.179	0.100	0.040	80.700	0.050	1.100	0.130	1.730	0.640	0.340	2.000
G23.99+00.49A	24.008	0.484	0.340	0.050	94.610	0.011	1.380	0.026	4.300	0.210	3.490	0.590
G24.14-00.16A	24.108	-0.167	0.510	0.049	80.900	0.014	1.350	0.035	2.020	0.160	0.340	0.410
G24.08+00.04A	24.154	0.078	0.310	0.077	51.880	0.014	1.010	0.035	4.350	0.360	0.670	1.800
G24.33+00.11B	24.334	0.149	0.680	0.053	114.210	0.013	1.760	0.030	2.590	0.120	0.890	0.240
G24.36-00.16A	24.366	-0.159	0.320	0.025	55.880	0.021	2.170	0.046	1.580	0.140	2.820	0.870
G24.37-00.21A	24.378	-0.212	0.190	0.039	55.290	0.046	1.850	0.120	1.480	0.350	6.550	2.500
G24.49-00.69A	24.489	-0.696	0.460	0.023	48.390	0.015	2.520	0.033	1.760	0.085	1.040	0.450

continued on next page

continued from previous page

Source	Gal. Long.	Gal. Lat.	T^1_{ant}	±	$v_{LSR,1}$	±	Δv^1	±	τ^{11}	±	τ^{22}	±
	deg		K			km s^{-1}						
G24.55-00.53C	24.541	-0.517	0.170	0.029	61.140	0.036	1.700	0.092	1.760	0.280	1.350	1.800
G24.54-00.73A	24.551	-0.741	0.180	0.030	48.560	0.032	1.460	0.087	1.100	0.300	0.150	18.000
G24.60+00.08A	24.628	0.154	0.590	0.044	53.090	0.013	1.760	0.030	2.090	0.120	1.000	0.390
G25.04-00.20G	24.916	-0.132	0.420	0.038	48.000	0.017	1.770	0.038	2.010	0.150	1.400	0.630
G25.04-00.20E	24.921	-0.157	0.650	0.037	47.260	0.010	1.540	0.020	2.310	0.092	1.880	0.460
G25.04-00.20D	25.151	-0.292	0.580	0.029	63.800	0.009	1.500	0.018	2.120	0.083	0.100	0.330
G25.04-00.20C	25.164	-0.311	0.420	0.023	63.410	0.013	1.860	0.026	2.250	0.091	0.870	0.540
G25.79+00.81A	25.784	0.803	0.110	0.029	49.010	0.068	2.800	0.140	2.250	0.430	5.270	2.900
G26.99+00.20G	26.851	0.179	0.320	0.054	93.890	0.019	1.260	0.043	2.780	0.270	1.930	0.980
G26.99+00.20B	26.949	0.183	0.180	0.046	92.620	0.037	1.350	0.099	2.010	0.420	4.910	2.700
G26.99+00.20A	27.014	0.199	0.310	0.043	94.140	0.018	1.690	0.039	3.170	0.210	3.400	1.100
G26.99+00.20A	27.014	0.199	0.310	0.055	94.190	0.025	1.680	0.055	2.910	0.270	0.100	0.190
G27.75+00.16A	27.741	0.171	0.290	0.053	78.220	0.022	1.350	0.049	2.600	0.290	6.410	2.000
G27.84+00.02A	27.784	0.068	0.460	0.036	101.050	0.016	1.650	0.038	1.520	0.140	1.470	0.930
G27.94-00.47A	27.954	-0.472	0.170	0.037	45.460	0.036	1.300	0.085	1.440	0.400	9.830	4.300
G28.04-00.46A	28.046	-0.466	0.430	0.048	45.660	0.016	1.450	0.036	2.370	0.180	0.200	2.600
G28.23-00.19A	28.273	-0.167	0.470	0.060	79.710	0.019	2.150	0.040	3.550	0.190	0.100	0.075
G28.28-00.34A	28.284	-0.347	0.610	0.051	48.700	0.009	1.530	0.019	3.550	0.130	0.550	0.450
G28.37+00.07B	28.376	0.053	0.520	0.038	79.700	0.015	1.990	0.031	2.230	0.120	1.570	0.830
G28.37+00.07E	28.388	0.036	0.510	0.052	79.010	0.018	1.810	0.041	2.240	0.160	0.100	0.350
G28.37+00.07C	28.398	0.084	0.990	0.061	78.130	0.012	2.280	0.026	3.070	0.098	0.640	0.270
G28.53-00.25B	28.538	-0.276	0.560	0.065	88.380	0.016	1.330	0.036	2.300	0.190	2.910	1.100
G28.53-00.25C	28.541	-0.241	0.420	0.050	86.740	0.031	2.030	0.074	1.500	0.210	0.460	1.300
G28.53-00.25A	28.563	-0.232	0.630	0.130	86.600	0.025	2.840	0.045	4.900	0.310	1.890	0.290
G29.27-00.71A	29.244	-0.677	0.190	0.053	83.210	0.048	1.390	0.110	2.210	0.480	3.010	3.300
G29.27-00.71B	29.286	-0.631	0.170	0.046	120.080	0.047	1.100	0.120	0.830	0.540	1.690	3.000
G31.22+00.01A	31.224	0.021	0.450	0.050	75.630	0.018	1.600	0.041	2.320	0.180	0.100	0.280
G31.97+00.07C	31.961	0.061	0.440	0.120	96.480	0.083	2.110	0.250	1.060	0.470	1.690	2.800
G31.97+00.07B	31.943	0.074	0.340	0.052	96.470	0.050	2.730	0.100	1.680	0.260	0.100	0.250
G33.69-00.01B	33.663	-0.032	0.140	0.039	104.930	0.095	2.540	0.240	1.720	0.460	0.700	1.500

continued on next page

continued from previous page

Source	Gal. Long.	Gal. Lat.	T^1_{ant}	±	$v_{LSR,1}$	±	Δv^1	±	τ^{11}	±	τ^{22}	±
	deg		K			km s^{-1}						
G33.69-00.01A	33.743	-0.012	0.320	0.074	50.540	0.035	1.940	0.068	3.160	0.360	2.430	0.870
G34.12+00.06A	34.131	0.073	0.210	0.037	56.980	0.043	1.800	0.120	1.150	0.320	1.580	1.800
G34.43+00.24A	34.431	0.241	0.520	0.049	57.920	0.027	2.250	0.065	1.310	0.170	0.800	1.000
G34.77-00.55A	34.781	-0.562	0.530	0.038	41.850	0.018	1.960	0.044	1.450	0.130	0.430	0.590
G34.88+00.29A	34.844	0.323	0.250	0.037	54.290	0.023	1.170	0.058	1.450	0.260	4.420	2.400
G34.91+00.13A	34.931	0.136	0.150	0.027	42.170	0.028	1.280	0.072	1.360	0.310	4.830	2.100
G35.19-00.72A	35.201	-0.726	0.990	0.290	32.570	0.043	1.100	0.110	1.160	0.540	0.610	0.390
G35.28-00.90A	35.291	-0.911	0.390	0.040	36.720	0.017	1.420	0.038	1.780	0.180	1.290	1.200
G35.39-00.33B	35.473	-0.314	0.680	0.077	45.030	0.010	1.070	0.023	3.060	0.170	1.620	0.910
G35.39-00.33A	35.478	-0.299	0.820	0.069	45.050	0.013	1.430	0.032	1.920	0.140	1.100	0.640
G35.59-00.24B	35.599	-0.261	0.250	0.029	43.880	0.043	2.440	0.130	0.200	0.250	4.020	1.500
G35.59-00.24A	35.604	-0.247	0.520	0.072	44.680	0.020	1.250	0.049	1.780	0.230	0.980	1.800
G36.67-00.11A	36.668	-0.116	0.300	0.048	53.350	0.028	1.280	0.067	1.340	0.290	2.460	1.500
G38.35-00.90A	38.359	-0.902	0.810	0.041	16.540	0.006	0.940	0.013	2.200	0.083	0.390	0.860
G42.26-00.54A	42.258	-0.556	0.250	0.034	72.260	0.031	1.530	0.073	0.950	0.260	10.140	3.900
G48.65-00.29A	48.658	-0.289	0.430	0.063	33.310	0.022	1.220	0.056	1.610	0.250	14.890	2.600
G19.89-00.61A	19.903	-0.586	0.130	0.042	24.090	0.055	1.270	0.130	1.330	0.590	0.000	0.000
G22.29-00.62A	22.308	-0.627	0.330	0.049	49.110	0.033	1.940	0.087	1.860	0.250	0.000	0.000
G22.35+00.41C	22.364	0.383	0.490	0.051	84.370	0.022	1.790	0.050	1.630	0.180	0.000	0.000
G22.56-00.20D	22.489	-0.209	0.320	0.045	75.690	0.030	1.510	0.073	1.160	0.260	0.000	0.000
G24.55-00.53A	24.486	-0.521	0.180	0.029	61.850	0.031	1.430	0.075	1.240	0.300	0.000	0.000
G24.60+00.08B	24.659	0.163	0.340	0.041	53.660	0.012	1.030	0.029	2.410	0.190	0.000	0.000
G25.04-00.20B	25.013	-0.184	0.190	0.025	46.230	0.036	1.660	0.092	0.670	0.270	0.000	0.000
G25.04-00.20F	25.044	-0.184	0.190	0.032	46.680	0.022	1.130	0.053	1.840	0.280	0.000	0.000
G26.99+00.20E	26.924	0.179	0.250	0.091	93.680	0.083	1.970	0.330	1.200	0.590	0.000	0.000
G28.23-00.19C	28.283	-0.146	0.300	0.035	81.070	0.028	1.850	0.070	1.420	0.200	0.000	0.000
G28.37+00.07D	28.364	0.079	0.490	0.051	80.530	0.028	2.190	0.068	1.710	0.180	0.000	0.000
G28.37+00.07G	28.366	0.121	0.390	0.059	81.590	0.020	1.480	0.043	2.800	0.240	0.000	0.000
G28.38-00.11A	28.391	-0.116	0.130	0.038	81.470	0.064	1.380	0.150	0.710	0.600	0.000	0.000
G28.37+00.07F	28.403	0.064	0.490	0.038	79.430	0.015	1.940	0.033	2.210	0.130	0.000	0.000

continued on next page

continued from previous page

Source	Gal. Long.	Gal. Lat.	T^1_{ant}	±	$v_{\rm LSR,1}$	±	Δv^1	±	τ^{11}	±	τ^{22}	±
	deg		K			km s^{-1}						
G28.53-00.25D	28.444	-0.316	0.270	0.072	47.180	0.036	1.060	0.098	1.330	0.480	0.000	0.000
G30.57-00.23A	30.576	-0.251	0.150	0.043	85.680	0.036	1.030	0.090	1.650	0.510	0.000	0.000
G31.97+00.07A	32.009	0.054	0.480	0.085	40.520	0.054	2.600	0.120	2.040	0.290	0.000	0.000
G34.34-00.72A	34.348	-0.727	0.250	0.048	11.330	0.020	0.720	0.049	1.400	0.360	0.000	0.000
G34.37-00.95C	34.453	-0.984	0.120	0.039	13.040	0.065	1.470	0.130	1.310	0.600	0.000	0.000
G35.14-00.02A	35.121	-0.009	0.200	0.064	27.720	0.028	0.880	0.066	2.420	0.520	0.000	0.000
G36.67-00.11A	36.668	-0.116	0.410	0.055	53.400	0.016	1.210	0.040	2.300	0.210	0.000	0.000
G38.33-00.81A	38.336	-0.804	0.300	0.064	16.800	0.014	0.710	0.031	3.060	0.330	0.000	0.000
G38.77+00.78A	38.779	0.789	0.150	0.055	33.600	0.042	0.960	0.120	1.630	0.610	0.000	0.000
G38.92-00.33A	38.904	-0.347	0.190	0.023	37.850	0.049	2.250	0.120	0.590	0.240	0.000	0.000
G38.95-00.47A	38.959	-0.469	0.810	0.029	42.170	0.009	1.820	0.020	1.530	0.062	0.000	0.000
G48.52-00.47A	48.519	-0.467	0.140	0.025	37.850	0.049	1.950	0.110	0.960	0.330	0.000	0.000

Table 2: Initial Conditions and Distances of detected IRDCs

Source	T_{rot}	±	N[NH_3]	±	Distance d	±	Radius r	±
	K		10^{15} cm^{-2}		kpc		pc	
G15.05+00.07A	11.980	1.311	5.285	8.027	2.568	0.620	0.498	0.097
G17.33+00.88A	10.424	9.121	3.328	61.771	1.825	0.710	0.354	0.069
G19.27+00.07A	8.902	1.892	10.504	81.329	1.970	0.658	0.382	0.074
G19.27+00.07B	27.263	12.247	8.716	9.623	1.896	0.670	0.368	0.071
G19.27-00.39A	14.659	2.048	1.360	1.524	3.452	0.461	0.669	0.130
G19.73-00.66A	13.515	1.548	1.625	1.838	1.703	0.694	0.330	0.064
G19.91-00.20A	20.347	5.300	5.989	6.487	3.839	0.421	0.744	0.144
G19.91-00.20A	21.211	5.329	4.129	3.838	3.838	0.421	0.744	0.144
G19.92-00.29A	20.500	2.260	11.161	4.606	3.907	0.414	0.758	0.147
G19.92-00.29A	24.497	3.191	11.667	4.093	3.912	0.414	0.758	0.147
G22.24-00.63A	17.637	3.180	2.082	1.974	2.960	0.515	0.574	0.111
G22.35+00.41B	23.454	14.099	0.243	0.529	4.467	0.389	0.866	0.168
G22.35+00.41A	14.241	1.805	3.266	3.555	3.184	0.493	0.617	0.120
G22.56-00.20F	13.238	1.529	2.030	2.444	4.152	0.410	0.805	0.156
G22.73+00.11A	15.570	2.381	3.138	3.361	4.222	0.408	0.819	0.159
G23.06+00.04A	14.813	2.287	6.601	8.010	4.691	0.388	0.910	0.176
G23.22-00.37A	28.580	3.921	17.050	4.968	4.180	0.415	0.810	0.157
G23.42-00.52A	12.300	1.540	16.476	26.524	3.622	0.457	0.702	0.136
G23.60+00.00A	10.705	0.967	11.150	19.646	3.150	0.499	0.611	0.118
G23.71+00.30A	14.482	2.242	2.657	3.497	5.352	0.393	1.038	0.201
G23.71+00.30B	17.010	4.135	1.087	1.592	4.540	0.402	0.880	0.171
G23.87+00.07A	13.662	1.723	4.697	5.683	3.161	0.499	0.613	0.119
G23.86-00.19A	24.798	9.120	2.133	2.361	4.264	0.418	0.827	0.160
G23.99+00.49A	11.140	1.113	18.998	32.662	4.774	0.401	0.926	0.180
G24.14-00.16A	12.011	4.192	4.315	20.642	4.261	0.421	0.826	0.160
G24.08+00.04A	11.401	1.346	13.862	26.301	3.037	0.512	0.589	0.114
G24.33+00.11B	22.685	3.177	6.776	2.922	5.459	0.416	1.058	0.205
G24.36-00.16A	13.924	1.604	4.129	4.333	3.210	0.497	0.622	0.121
G24.37-00.21A	17.232	2.941	2.884	2.707	3.182	0.500	0.617	0.120
G24.49-00.69A	19.446	5.313	5.053	5.754	2.845	0.531	0.552	0.107

continued on next page

continued from previous page

Source	T_{rot}	±	N[NH_3]	±	Distance d	±	Radius r	±
	K		10^{15} cm^{-2}		kpc		pc	
G24.55-00.53C	17.560	3.025	3.479	3.124	3.434	0.479	0.666	0.129
G24.54-00.73A	18.526	3.454	1.431	1.230	2.850	0.531	0.553	0.107
G24.60+00.08A	17.397	3.991	4.810	5.821	3.069	0.511	0.595	0.115
G25.04-00.20G	12.274	1.232	5.499	7.103	2.807	0.537	0.544	0.106
G25.04-00.20E	20.636	2.397	4.858	2.083	2.770	0.541	0.537	0.104
G25.04-00.20D	9.095	6.537	7.499	181.744	3.520	0.477	0.683	0.132
G25.04-00.20C	13.852	3.378	6.391	14.353	3.503	0.479	0.679	0.132
G25.79+00.81A	21.525	5.942	8.418	8.200	2.820	0.540	0.547	0.106
G26.99+00.20G	12.494	1.430	6.808	9.570	4.675	0.459	0.906	0.176
G26.99+00.20B	16.619	2.929	3.502	3.738	4.623	0.461	0.896	0.174
G26.99+00.20A	12.258	1.344	11.820	16.779	4.682	0.463	0.908	0.176
G26.99+00.20A	8.016	2.889	18.849	367.418	4.684	0.463	0.908	0.176
G27.75+00.16A	13.079	1.608	6.231	8.291	4.030	0.484	0.781	0.152
G27.84+00.02A	12.508	1.253	3.197	3.918	4.950	0.493	0.960	0.186
G27.94-00.47A	18.247	3.443	1.915	1.782	2.540	0.576	0.492	0.095
G28.04-00.46A	11.830	1.166	6.194	8.754	2.546	0.576	0.494	0.096
G28.23-00.19A	7.668	1.059	38.661	344.800	4.076	0.492	0.790	0.153
G28.28-00.34A	10.129	2.141	16.431	80.914	2.689	0.566	0.521	0.101
G28.37+00.07B	11.358	1.026	7.971	11.666	4.075	0.494	0.790	0.153
G28.37+00.07E	8.961	6.663	10.212	270.118	4.046	0.495	0.785	0.152
G28.37+00.07C	11.272	1.524	16.334	36.619	4.010	0.496	0.777	0.151
G28.53-00.25B	11.081	1.006	5.778	9.173	4.428	0.496	0.859	0.166
G28.53-00.25C	12.875	1.389	3.761	4.560	4.361	0.495	0.846	0.164
G28.53-00.25A	22.564	1.976	36.472	10.843	4.355	0.496	0.844	0.164
G29.27-00.71A	15.885	2.765	4.312	5.083	4.201	0.510	0.815	0.158
G29.27-00.71B	19.734	6.506	0.719	1.029	5.849	0.098	1.134	0.220
G31.22+00.01A	8.858	5.281	9.796	216.624	3.857	0.556	0.748	0.145
G31.97+00.07C	13.294	2.021	2.265	3.643	4.816	0.650	0.934	0.181
G31.97+00.07B	9.859	5.787	8.147	121.917	4.815	0.649	0.934	0.181
G33.69-00.01B	19.542	4.271	4.902	4.688	5.372	0.074	1.042	0.202

continued on next page

continued from previous page

Source	T_{rot}	±	N[NH_3]	±	Distance d	±	Radius r	±
	K		10^{15} cm^{-2}		kpc		pc	
G33.69-00.01A	12.149	1.471	13.599	21.968	2.636	0.630	0.511	0.099
G34.12+00.06A	17.169	2.904	1.917	1.775	2.952	0.626	0.572	0.111
G34.43+00.24A	12.327	1.229	3.508	4.462	2.997	0.631	0.581	0.113
G34.77-00.55A	14.653	7.395	3.162	12.706	2.165	0.667	0.420	0.081
G34.88+00.29A	15.431	2.151	1.840	1.798	2.813	0.643	0.545	0.106
G34.91+00.13A	19.660	3.947	1.704	1.404	2.186	0.668	0.424	0.082
G35.19-00.72A	17.819	5.916	1.175	2.031	1.650	0.703	0.320	0.062
G35.28-00.90A	12.813	1.361	3.475	4.206	1.876	0.689	0.364	0.071
G35.39-00.33B	10.040	0.816	8.810	17.186	2.324	0.669	0.451	0.087
G35.39-00.33A	17.051	5.748	3.407	6.338	2.325	0.669	0.451	0.087
G35.59-00.24B	18.108	11.457	0.292	1.070	2.262	0.673	0.439	0.085
G35.59-00.24A	11.794	1.170	3.294	4.733	2.304	0.672	0.447	0.087
G36.67-00.11A	14.612	1.939	1.832	1.955	2.747	0.680	0.533	0.103
G38.35-00.90A	10.203	0.797	4.193	7.454	0.648	0.806	0.126	0.024
G42.26-00.54A	16.384	2.562	1.258	1.197	3.967	0.002	0.769	0.149
G48.65-00.29A	12.647	1.377	2.565	3.306	1.660	1.001	0.322	0.062
G19.89-00.61A	21.447	6.088	1.623	1.798	1.729	0.688	0.335	0.065
G22.29-00.62A	13.401	1.581	4.936	5.879	3.012	0.509	0.584	0.113
G22.35+00.41C	12.155	1.205	3.974	5.218	4.479	0.389	0.868	0.168
G22.56-00.20D	14.581	1.904	1.743	1.836	4.145	0.410	0.804	0.156
G24.55-00.53A	18.199	3.239	1.678	1.434	3.467	0.476	0.672	0.130
G24.60+00.08B	12.634	1.374	4.270	5.508	3.094	0.509	0.600	0.116
G25.04-00.20B	19.114	4.495	0.820	0.853	2.714	0.546	0.526	0.102
G25.04-00.20F	16.528	2.627	2.534	2.409	2.735	0.544	0.530	0.103
G26.99+00.20E	15.888	3.197	2.295	3.286	4.665	0.460	0.905	0.175
G28.23-00.19C	14.483	1.799	2.908	2.966	4.132	0.491	0.801	0.155
G28.37+00.07D	12.065	1.187	5.289	7.042	4.110	0.493	0.797	0.155
G28.37+00.07G	11.768	1.216	8.561	12.914	4.154	0.493	0.806	0.156
G28.38-00.11A	23.216	14.401	0.727	1.432	4.147	0.493	0.804	0.156
G28.37+00.07F	11.559	1.071	7.510	10.686	4.064	0.495	0.788	0.153

continued on next page

continued from previous page

Source	T_{rot}	±	N[NH_3]	±	Distance d	±	Radius r	±
	K		10^{15} cm^{-2}		kpc		pc	
G28.53-00.25D	15.196	2.477	1.470	1.824	2.608	0.574	0.506	0.098
G30.57-00.23A	18.966	4.025	1.867	1.879	4.302	0.547	0.834	0.162
G31.97+00.07A	11.788	1.230	8.604	13.057	2.159	0.638	0.419	0.081
G34.34-00.72A	15.519	2.314	1.070	1.120	0.367	0.816	0.071	0.014
G34.37-00.95C	22.649	7.274	1.834	2.081	0.477	0.804	0.093	0.018
G35.14-00.02A	15.223	2.688	3.259	4.306	1.381	0.724	0.268	0.052
G36.67-00.11A	12.059	1.242	4.815	6.728	2.750	0.680	0.533	0.103
G38.33-00.81A	12.481	1.526	4.578	6.912	0.666	0.805	0.129	0.025
G38.77+00.78A	19.012	4.345	1.706	1.913	1.673	0.748	0.324	0.063
G38.92-00.33A	19.322	4.734	0.943	1.053	1.899	0.740	0.368	0.071
G38.95-00.47A	10.755	0.877	4.162	6.562	2.137	0.735	0.414	0.080
G48.52-00.47A	21.516	5.567	1.547	1.365	1.953	1.031	0.379	0.073

Table 3: Flux Densities Masses of detected IRDCs

Source	F_ν	M_{vir}	±	M_{gas}	±	M_{MRN}	±	α_{gas}	α_{MRN}
	Jy			$M_\odot$				$\kappa_\nu = 1.85$ cm^2 g^{-1}	$\kappa_{MRN} = 0.589$
G15.05+00.07A	0.637	81.839	16.575	53.543	30.002	168.086	97.885	1.528	0.487
G17.33+00.88A	2.012	157.782	31.956	111.549	214.476	350.186	675.589	1.414	0.451
G19.27+00.07A	1.949	204.351	41.388	175.363	147.344	550.517	470.723	1.165	0.371
G19.27+00.07B	0.471	938.930	190.163	6.049	5.735	18.991	18.254	155.212	49.442
G19.27-00.39A	1.194	130.303	26.390	127.353	51.830	399.798	174.623	1.023	0.326
G19.73-00.66A	1.151	89.547	18.136	34.318	29.587	107.734	94.440	2.609	0.831
G19.91-00.20A	0.736	508.904	103.069	58.260	28.122	182.895	92.924	8.735	2.782
G19.91-00.20A	0.736	437.961	88.701	54.802	25.653	172.038	85.029	7.992	2.546
G19.92-00.29A	3.738	1055.869	213.847	303.093	100.910	951.497	350.882	3.484	1.110
G19.92-00.29A	3.738	1078.544	218.439	236.100	80.739	741.188	279.387	4.568	1.455
G22.24-00.63A	0.367	249.910	50.615	21.402	10.447	67.186	34.483	11.677	3.720
G22.35+00.41B	1.458	656.406	132.943	127.568	112.139	400.473	357.718	5.146	1.639
G22.35+00.41A	2.793	370.936	75.126	266.087	113.416	835.325	379.888	1.394	0.444
G22.56-00.20F	0.543	177.095	35.867	99.717	34.531	313.041	119.228	1.776	0.566
G22.73+00.11A	1.010	457.147	92.587	145.912	54.399	458.060	185.579	3.133	0.998
G23.06+00.04A	1.280	396.019	80.206	247.755	90.383	777.776	309.386	1.598	0.509
G23.22-00.37A	9.652	648.287	131.299	565.688	189.361	1775.863	657.786	1.146	0.365
G23.42-00.52A	1.776	392.228	79.439	283.105	111.618	888.750	377.681	1.385	0.441
G23.60+00.00A	2.175	272.404	55.170	341.016	141.418	1070.551	475.302	0.799	0.254
G23.71+00.30A	0.408	232.193	47.026	106.753	38.349	335.128	131.596	2.175	0.693
G23.71+00.30B	0.976	272.603	55.211	141.589	65.805	444.490	218.274	1.925	0.613
G23.87+00.07A	0.434	119.303	24.163	43.731	18.922	137.283	63.264	2.728	0.869
G23.86-00.19A	0.562	158.078	32.016	41.484	23.919	130.232	77.878	3.811	1.214
G23.99+00.49A	1.453	278.552	56.416	484.259	156.903	1520.234	548.392	0.575	0.183
G24.14-00.16A	1.962	237.924	48.187	452.094	317.325	1419.257	1021.282	0.526	0.168
G24.08+00.04A	1.334	94.919	19.224	172.139	77.726	540.394	258.613	0.551	0.176
G24.33+00.11B	3.859	518.042	104.920	528.298	168.846	1658.484	591.713	0.981	0.312
G24.36-00.16A	1.545	463.100	93.792	155.428	64.962	487.933	218.120	2.980	0.949
G24.37-00.21A	0.743	333.646	67.574	51.894	23.731	162.910	78.850	6.429	2.048
G24.49-00.69A	3.130	553.501	112.101	145.432	85.324	456.553	277.469	3.806	1.212

continued on next page

continued from previous page

Source	F_ν	$M_{\rm vir}$	±	M_{gas}	±	M_{MRN}	±	α_{gas}	α_{MRN}
	Jy			$M_\odot$				$\kappa_\nu = 1.85$ cm^2 g^{-1}	$\kappa_{MRN} = 0.589$
G24.55-00.53C	1.070	304.005	61.571	84.511	36.706	265.304	122.671	3.597	1.146
G24.54-00.73A	0.558	186.094	37.690	27.970	14.217	87.808	46.754	6.653	2.119
G24.60+00.08A	2.861	291.241	58.986	183.148	96.488	574.957	316.329	1.590	0.507
G25.04-00.20G	1.740	269.420	54.566	167.214	78.392	524.934	259.793	1.611	0.513
G25.04-00.20E	2.077	201.261	40.762	83.835	39.401	263.182	130.541	2.401	0.765
G25.04-00.20D	2.586	242.645	49.143	708.714	1131.963	2224.864	3571.038	0.342	0.109
G25.04-00.20C	2.042	371.227	75.185	246.749	132.735	774.619	434.423	1.504	0.479
G25.79+00.81A	0.626	677.294	137.174	24.639	14.440	77.348	46.961	27.489	8.756
G26.99+00.20G	1.327	227.360	46.048	342.409	119.207	1074.923	411.216	0.664	0.212
G26.99+00.20B	0.342	258.151	52.284	53.375	21.164	167.560	71.556	4.837	1.541
G26.99+00.20A	1.347	409.675	82.972	360.975	124.548	1133.208	430.310	1.135	0.362
G26.99+00.20A	1.347	405.010	82.027	870.231	781.135	2731.911	2490.185	0.465	0.148
G27.75+00.16A	0.922	225.004	45.571	162.974	61.971	511.623	210.785	1.381	0.440
G27.84+00.02A	1.888	412.829	83.611	545.144	182.778	1711.368	634.733	0.757	0.241
G27.94-00.47A	0.283	131.486	26.630	11.529	6.604	36.193	21.512	11.405	3.633
G28.04-00.46A	0.606	164.001	33.215	51.271	27.043	160.954	88.649	3.199	1.019
G28.23-00.19A	2.417	577.250	116.911	1315.635	605.734	4130.168	2011.201	0.439	0.140
G28.28-00.34A	3.006	192.869	39.062	383.514	242.949	1203.963	786.220	0.503	0.160
G28.37+00.07B	1.544	494.426	100.137	361.254	129.374	1134.085	444.178	1.369	0.436
G28.37+00.07E	0.865	406.106	82.249	323.560	537.551	1015.751	1695.202	1.255	0.400
G28.37+00.07C	8.693	638.573	129.331	1997.730	818.159	6271.467	2754.251	0.320	0.102
G28.53-00.25B	1.785	239.971	48.602	517.002	179.670	1623.022	619.979	0.464	0.148
G28.53-00.25C	2.685	550.566	111.507	571.448	204.739	1793.944	702.874	0.963	0.307
G28.53-00.25A	6.671	1076.115	217.947	585.642	191.704	1838.504	668.711	1.837	0.585
G29.27-00.71A	1.230	248.693	50.368	170.370	71.802	534.842	240.834	1.460	0.465
G29.27-00.71B	0.306	216.819	43.913	58.796	31.021	184.579	101.687	3.688	1.175
G31.22+00.01A	1.111	302.517	61.269	387.375	528.181	1216.085	1669.292	0.781	0.249
G31.97+00.07C	0.895	656.894	133.042	219.571	94.063	689.300	314.871	2.992	0.953
G31.97+00.07B	1.006	1099.443	222.672	434.880	546.811	1365.216	1730.200	2.528	0.805
G33.69-00.01B	2.091	1061.860	215.060	343.906	131.305	1079.623	446.343	3.088	0.984

continued on next page

continued from previous page

Source	F_ν Jy	M_{vir}	±	M_{gas}	± ($M_\odot$)	M_{MRN}	±	α_{gas} $\kappa_\nu = 1.85$ cm^2 g^{-1}	α_{MRN} $\kappa_{MRN} = 0.589$
G33.69-00.01A	3.759	303.951	61.560	324.580	182.890	1018.951	596.448	0.936	0.298
G34.12+00.06A	0.976	293.031	59.348	59.012	31.743	185.256	103.891	4.966	1.582
G34.43+00.24A	2.322	464.827	94.142	252.371	126.234	792.268	415.722	1.842	0.587
G34.77-00.55A	1.752	254.753	51.596	73.525	78.127	230.817	247.981	3.465	1.104
G34.88+00.29A	0.581	117.964	23.891	37.806	20.728	118.683	67.739	3.120	0.994
G34.91+00.13A	0.304	109.702	22.218	8.201	5.812	25.746	18.696	13.377	4.261
G35.19-00.72A	4.518	61.152	12.385	80.527	81.608	252.799	259.310	0.759	0.242
G35.28-00.90A	0.990	115.907	23.475	39.337	30.858	123.490	98.831	2.947	0.939
G35.39-00.33B	1.226	81.511	16.508	118.933	75.117	373.365	243.134	0.685	0.218
G35.39-00.33A	2.070	145.656	29.500	78.467	63.199	246.331	202.210	1.856	0.591
G35.59-00.24B	0.602	412.601	83.565	19.687	22.675	61.803	71.855	20.958	6.676
G35.59-00.24A	1.134	110.307	22.341	79.037	50.858	248.121	164.435	1.396	0.445
G36.67-00.11A	1.093	137.907	27.931	74.246	42.939	233.079	139.772	1.857	0.592
G38.35-00.90A	1.370	17.544	3.553	10.004	25.026	31.404	78.723	1.754	0.559
G42.26-00.54A	0.479	284.485	57.617	56.285	17.953	176.696	62.940	5.054	1.610
G48.65-00.29A	0.919	75.707	15.333	29.268	36.210	91.881	114.605	2.587	0.824
G19.89-00.61A	0.719	85.438	17.304	10.695	9.799	33.575	31.219	7.989	2.545
G22.29-00.62A	1.278	347.257	70.331	120.902	53.616	379.547	178.752	2.872	0.915
G22.35+00.41C	2.619	439.631	89.039	652.199	209.435	2047.446	733.273	0.674	0.215
G22.56-00.20D	0.404	289.549	58.643	62.686	22.334	196.789	76.744	4.619	1.471
G24.55-00.53A	0.636	217.226	43.995	48.495	21.074	152.241	70.425	4.479	1.427
G24.60+00.08B	0.391	100.563	20.367	43.329	18.708	136.023	62.565	2.321	0.739
G25.04-00.20B	0.538	229.092	46.398	23.334	13.318	73.251	43.392	9.818	3.128
G25.04-00.20F	0.389	106.975	21.666	21.423	10.963	67.253	36.032	4.993	1.591
G26.99+00.20E	0.353	554.676	112.339	60.262	25.844	189.180	86.499	9.204	2.932
G28.23-00.19C	1.402	433.295	87.756	218.678	81.812	686.496	278.951	1.981	0.631
G28.37+00.07D	1.055	603.932	122.315	224.295	80.975	704.130	277.644	2.693	0.858
G28.37+00.07G	1.155	278.784	56.463	262.728	95.935	824.780	328.340	1.061	0.338
G28.38-00.11A	0.366	241.955	49.003	27.994	25.797	87.880	82.175	8.643	2.753
G28.37+00.07F	1.288	468.542	94.895	289.878	104.384	910.012	358.059	1.616	0.515

continued on next page

continued from previous page

Source	F_ν	M_{vir}	±	M_{gas}	±	M_{MRN}	±	α_{gas}	α_{MRN}
	Jy			$M_\odot$				$\kappa_\nu = 1.85$ cm^2 g^{-1}	$\kappa_{MRN} = 0.589$
G28.53-00.25D	0.322	89.786	18.185	18.473	10.202	57.993	33.321	4.860	1.548
G30.57-00.23A	0.914	139.820	28.318	100.789	45.731	316.406	152.078	1.387	0.442
G31.97+00.07A	3.613	447.087	90.549	221.213	144.496	694.452	466.791	2.021	0.644
G34.34-00.72A	0.543	5.836	1.182	0.598	2.659	1.876	8.354	9.768	3.111
G34.37-00.95C	0.432	31.599	6.400	0.453	1.542	1.423	4.848	69.728	22.211
G35.14-00.02A	0.587	32.764	6.636	9.414	10.408	29.553	33.007	3.480	1.109
G36.67-00.11A	1.093	123.352	24.983	104.125	58.965	326.879	192.229	1.185	0.377
G38.33-00.81A	0.385	10.280	2.082	2.018	4.919	6.336	15.473	5.093	1.622
G38.77+00.78A	0.225	47.247	9.569	3.741	3.658	11.743	11.633	12.631	4.023
G38.92-00.33A	0.943	294.586	59.663	19.716	17.417	61.894	55.550	14.942	4.760
G38.95-00.47A	2.994	216.850	43.919	214.016	157.103	671.859	504.569	1.013	0.323
G48.52-00.47A	0.381	227.570	46.090	7.201	8.186	22.605	25.948	31.603	10.067

Table 4: Initial conditions of HMPOs in NH_3

Source	T^1_{ant}	±	$v_{\rm LSR,1}$	±	Δv^1	±	τ^{11}	±	τ^{22}	±	T^1_{rot}	±	N[NH_3]
	K			km s^{-1}							K		10^{15} cm^{-2}
G05.358+3.543	0.73	0.00	-16.67	0.00	2.15	0.01	0.82	0.01	0.10	0.01	41.86	16.54	8.30
G05.490+2.658	0.14	0.01	0.27	0.02	1.45	0.06	0.32	0.18	0.10	0.05	25.77	11.55	0.76
G05.553+1.631	0.05	0.00	5.27	0.04	1.97	0.09	0.10	0.12	0.10	0.46	20.28	12.01	0.33
G22.134+5.834	0.24	0.01	-18.70	0.01	1.41	0.03	0.46	0.11	0.10	0.06	22.68	7.04	1.30
G22.570+5.912	0.10	0.01	-45.62	0.03	1.78	0.09	0.69	0.25	1.01	0.95	19.24	3.36	0.79
G23.033+5.951	0.37	0.00	-53.04	0.00	2.07	0.01	0.72	0.02	0.10	0.06	21.86	4.97	3.40
G23.139+5.939	0.15	0.01	-44.31	0.01	1.81	0.04	0.28	0.08	0.10	0.04	31.50	17.08	1.00
G23.151+5.912	0.04	0.01	-54.47	0.07	1.87	0.17	0.40	0.45	0.30	2.40	19.61	5.84	0.29
G23.545+6.508	0.08	0.01	-18.25	0.03	2.11	0.08	0.25	0.18	0.10	2.10	28.70	16.27	0.62
G20.216+4.107	0.26	0.01	-1.93	0.01	1.20	0.01	1.96	0.07	0.10	0.12	26.66	2.06	2.30
G20.293+3.952	0.96	0.06	5.67	0.01	1.56	0.03	1.68	0.10	0.10	0.00	31.80	3.99	10.00
G19.217+1.651	0.23	0.01	3.14	0.02	3.09	0.05	1.38	0.11	0.10	0.05	33.14	5.88	4.40
G18.089-1.732	0.56	0.00	32.42	0.00	2.99	0.01	2.43	0.00	1.37	0.14	24.39	0.43	14.00
G18.090-1.832	0.12	0.02	109.59	0.04	1.95	0.07	2.26	0.28	0.10	0.38	25.72	1.42	1.90
G18.151-1.208	0.40	0.02	32.48	0.01	1.86	0.03	1.30	0.08	0.10	0.11	41.87	10.11	4.80
G18.426-0.204	0.10	0.01	15.35	0.05	2.65	0.12	0.86	0.22	0.10	0.76	22.21	4.27	1.30
G18.431-0.312	0.17	0.03	103.94	0.04	1.69	0.10	1.19	0.30	0.10	0.12	26.14	4.22	1.60
G18.521+0.134	0.13	0.02	75.97	0.05	2.29	0.12	1.54	0.30	0.10	0.10	31.36	4.49	1.90
G18.530+0.215	0.46	0.03	76.35	0.03	2.26	0.06	0.95	0.12	0.16	0.00	29.57	7.21	5.30
G18.517+0.437	0.28	0.01	43.34	0.02	2.35	0.05	0.10	0.21	0.10	0.04	23.85	26.07	2.20
G19.035+0.641	0.18	0.01	32.13	0.03	3.46	0.07	0.68	0.12	0.74	0.45	21.69	4.58	2.70
G19.074+0.752	0.14	0.01	54.51	0.03	2.47	0.07	0.80	0.16	0.10	0.15	25.37	6.07	1.60
G19.220+1.432	0.18	0.01	68.99	0.02	2.44	0.05	1.20	0.11	1.55	0.56	17.78	1.77	2.50
G19.266+1.745	0.17	0.01	4.70	0.04	2.57	0.10	0.55	0.18	0.68	0.56	21.63	5.23	1.80
G19.282+1.814	0.30	0.02	22.53	0.01	1.22	0.03	0.98	0.14	0.10	0.54	26.21	5.28	1.80
G19.403+2.258	0.15	0.02	25.98	0.03	1.39	0.06	1.07	0.25	0.10	0.17	37.36	10.05	1.20
G19.471+2.641	0.18	0.02	22.42	0.03	1.59	0.07	0.94	0.22	0.10	0.39	28.90	6.81	1.40
G20.081+2.720	0.33	0.02	5.35	0.01	1.21	0.03	0.51	0.12	2.33	1.70	15.83	3.08	1.70
G20.051+3.435	0.07	0.01	11.21	0.08	3.27	0.21	0.12	0.63	0.43	2.80	17.31	16.43	0.80
G20.126+4.104	0.57	0.03	-4.01	0.01	1.86	0.03	1.65	0.09	0.10	0.14	45.03	8.16	8.00

continued on next page

continued from previous page

Source	T^1_{ant}	±	$v_{LSR,1}$	±	Δv^1	±	τ^{11}	±	τ^{22}	±	T^1_{rot}	±	N[NH_3]
	K			km s^{-1}								K	10^{15} cm^{-2}
G20.205+3.948	0.07	0.02	-2.28	0.06	1.56	0.18	0.74	0.57	0.10	0.88	26.77	7.36	0.50
G20.319+3.958	0.10	0.02	8.06	0.04	1.10	0.10	0.41	0.43	1.45	1.50	20.89	7.10	0.43
G20.332+4.124	0.17	0.02	-2.81	0.03	2.32	0.08	1.08	0.19	0.10	0.15	26.30	4.81	2.10
G20.343+4.129	0.16	0.01	10.98	0.03	2.42	0.06	1.57	0.17	2.14	0.90	20.18	1.51	2.50
G19.410+2.336	0.89	0.00	22.08	0.00	1.57	0.01	0.92	0.00	0.10	0.01	38.85	12.82	7.50
G18.159-1.550	0.40	0.03	59.15	0.02	1.98	0.04	1.55	0.12	0.10	0.08	29.19	3.75	5.10
G18.182-1.433	0.52	0.02	59.02	0.01	2.70	0.03	1.42	0.07	0.39	0.22	25.67	3.14	8.40
G18.264-1.152	0.68	0.03	42.81	0.01	2.23	0.03	1.06	0.08	0.10	0.04	40.78	12.26	8.80
G18.223-1.243	0.51	0.04	44.49	0.01	1.54	0.03	2.11	0.13	0.14	0.40	32.21	2.40	6.30
G18.272-1.217	0.12	0.02	33.61	0.04	1.69	0.13	1.16	0.30	0.10	0.41	21.65	2.83	1.10
G18.290-0.924	0.48	0.03	83.33	0.01	1.79	0.03	2.04	0.11	0.22	0.21	23.42	1.38	6.40
G18.102-1.800	0.91	0.06	21.17	0.02	2.34	0.04	2.14	0.11	0.10	0.36	56.13	7.90	21.00
G18.306-0.835	0.65	0.03	77.07	0.01	1.99	0.02	2.03	0.09	0.66	0.25	22.34	1.24	9.60
G18.308-0.841	0.60	0.10	75.59	0.02	1.78	0.05	2.93	0.24	0.70	0.30	23.24	0.75	11.00
G18.310-0.825	0.60	0.05	83.14	0.01	1.54	0.03	2.48	0.13	0.70	0.24	23.41	0.91	8.00
G18.337-0.743	0.94	0.06	57.58	0.02	2.56	0.03	2.57	0.11	0.60	0.18	23.41	0.85	21.00
G18.345-0.641	0.36	0.04	94.21	0.00	1.55	0.06	1.75	0.21	0.10	0.53	37.61	5.12	4.10
G18.372-0.541	0.14	0.02	22.42	0.08	3.44	0.20	0.50	0.28	1.51	0.02	17.62	4.07	2.00
G18.385-0.512	0.08	0.01	25.09	0.10	4.03	0.24	0.20	0.32	0.10	1.30	21.98	12.18	1.10
G18.460-0.307	0.37	0.03	82.28	0.01	1.43	0.03	1.64	0.13	0.52	0.39	18.64	1.24	3.50
G18.440-0.148	0.30	0.03	96.40	0.02	1.58	0.04	1.86	0.16	0.85	0.39	20.05	1.12	3.30
G18.445-0.222	0.26	0.02	85.99	0.03	2.79	0.06	0.93	0.13	1.56	0.40	19.24	2.82	3.60
G18.447-0.229	0.30	0.02	101.45	0.02	1.67	0.04	1.48	0.15	0.10	0.18	23.94	2.63	3.10
G18.454-0.136	0.21	0.02	38.42	0.03	1.86	0.09	0.79	0.22	0.98	1.70	17.66	2.82	1.90
G18.470-0.044	0.26	0.03	94.89	0.03	2.23	0.09	0.61	0.19	0.10	0.31	32.02	12.19	2.60
G18.472-0.022	0.32	0.02	49.03	0.02	2.36	0.04	1.42	0.11	0.10	0.12	23.35	2.71	4.50
G18.488+0.000	0.28	0.03	81.92	0.03	2.33	0.09	0.90	0.20	0.10	0.05	35.06	10.75	3.40
G18.553+0.414	0.09	0.02	10.22	0.09	3.55	0.22	0.69	0.33	0.59	1.10	19.32	3.32	1.40
G18.566+0.408	0.49	0.05	83.94	0.02	1.85	0.05	2.18	0.17	0.10	0.09	38.13	3.66	7.80
G19.012+0.536	0.16	0.01	65.44	0.04	2.59	0.11	0.15	0.17	0.10	0.25	21.18	11.57	1.40

continued on next page

continued from previous page

Source	T^1_{ant}	±	$v_{\mathrm{LSR},1}$	±	Δv^1	±	τ^{11}	±	τ^{22}	±	T^1_{rot}	±	N[NH_3]
	K			km s^{-1}								K	10^{15} cm^{-2}
G19.411+2.306	0.19	0.01	28.77	0.02	2.12	0.06	0.44	0.14	0.10	1.80	20.08	5.53	1.60
G19.413+2.332	0.39	0.01	20.22	0.01	1.88	0.02	1.20	0.07	0.10	0.19	25.02	3.97	4.00
G18.247-1.147	0.24	0.03	119.72	0.03	2.08	0.06	2.34	0.23	0.10	0.21	30.89	2.11	4.30
G18.454-0.158	0.31	0.06	99.24	0.02	1.58	0.05	3.24	0.27	0.54	0.37	19.52	0.45	5.30
G18.437-0.216	0.28	0.05	95.23	0.04	2.00	0.11	1.52	0.29	0.62	0.70	16.24	0.94	3.70

List of Figures

List of Tables

Bibliography

References

Bertoldi, F. et al. (1992). "Pressure-confined clumps in magnetized molecular clouds". In: *ApJ* 395, pp. 140–157.

Beuther, H. (1999). "On the Fly Kartierung und Multilinienanalyse der interstellaren Molekülwolke Cepheus B". PhD thesis.

– (2002). "Early Stages of Massive Star Formation". PhD thesis.

– (2008). *EF08C001: A COMPLETE Contrast-limited Sample of IRDCs.*

Beuther, H. et al. (2007). "The Formation of Massive Stars". In: *Protostars and Planets V*, 165–180.

Bonnell, I. A. et al. (1998). "On the formation of massive stars". In: *MNRAS* 298, 93–102.

Ho, P. T. P. (1977). "Study of the Ammonia Molecule in the Interstellar Medium". PhD thesis.

Ho, P. T. P. et al. (1983). "Interstellar Ammoniak". In: *A&A* 21, 239–270.

Jijina, J. et al. (1996). "Infall Collapse Solutions in the Inner Limit: Radiation Pressure and Its Effects on Star Formation". In: *AphJ* 462, 874ff.

Jijina, J. et al. (Nov. 1999). "Dense Cores Mapped in Ammonia: A Database". In: *ApJS* 125, pp. 161–236.

Kraus, J. D. (1986). *Radio Astronomy.* 2nd. Cygnus-Quasar Books.

MacLaren, I. et al. (1988). "Corrections to Virial Estimates of Molecular Cloud Masses". In: *AphJ* 333, 821–825.

Mathis, J. S. et al. (1977). "The size distribution of interstellar grains". In: *ApJ* 217, 425–433.

Muench, A. A. et al. (2002). "The Luminosity and Mass Function of the Trapezium Cluster: From B Stars to the Deuterium-burning Limit". In: *AphJ* 573, 366–393.

Norberg, P. et al. (2000). "On the Formation of Massive Stars by Accretion". In: *A&A* 359, 1025–1034.

Ossenkopf, V. et al. (1994). "Dust opacities for protostellar cores". In: *A&A* 291, 943–959.

Pallai, F. et al. (1999). "Star Formation in the Orion Nebula Cluster". In: *ApJ* 525, 772–783.

Pillai, T. et al. (2006). "Ammonia in Infrared Dark Clouds". In: *A&A* 450, 569–583.

Reid, M. J. et al. (2009). "Trigonometric Parallaxes of Massive Star-forming Regions. VI. Galactic Structure, Fundamental Parametersand Noncircular Motions". In: *ApJ* 700, 137–14.

Schilke, P. (1989). "Ammoniak in warmen Molekülwolken". PhD thesis.

Schuller, F. et al. (2009). “ATLASGAL - The APEX Telescope Large Area Survey of the Galaxy at 870um”. In: *A&A* 504, 415–427.

Simon, R. et al. (2006). “A Catalog of Midcourse Space Experiment Infrared Dark Cloud Candidates”. In: *AphJ* 639, 227–23.

Sridharan, T. K. et al. (Feb. 2002). “High-Mass Protostellar Candidates. I. The Sample and Initial Results”. In: *ApJ* 566, pp. 931–944.

Sridharan, T. K. et al. (2005). “High-Mass Starless Cores”. In: *AphJ* 634.

Stahler, S. W. et al. (2000). “The Formation of Massive Stars”. In: *Protostars and Planets IV*, 327ff.

Tan, J. C. et al. (2002). “The Formation of Massive Stars and Star Clusters”. In: *Hot Star Workshop III: The Earliest Phases of Massive Star Birth.* Ed. by P. Crowther. Vol. 267. Astronomical Society of the Pacific Conference Series, 267ff.

Townes, C. H. et al. (1975). *Microwave spectroscopy.* Ed. by C. H. & Schawlow A. L. Townes.

Ward-Thompson, D. et al. (2011). *An Introduction to Star Formation.* 1st. Cambridge University Press.

Wolfire, M. G. et al. (1987). “Conditions for the formation of massive stars”. In: *AphJ* 319, 850–867.

Yorke, H. W. (2002). “Theory of Formation of Massive Stars via Accretion”. In: *Hot Star Workshop III: The Earliest Phases of Massive Star Birth.* Ed. by P. Crowther. Vol. 267. Astronomical Society of the Pacific Conference Series, 165ff.

Zinnecker, H. et al. (2002). “Proceedings of "The earliest stages of massive star formation"”. In: *ASP Conf. Series.*

Weblinks

Antonine Education. *The Spectrum of Electromagnetic Waves.* URL: `http://www.antonine-education.co.uk/physics_gcse/Unit_1/Topic_5/topic_5_what_are_the_uses_and_ha.htm`.

Buisson, G. et al. (2007). *GILDAS GreG Documentation.* URL: `http://www.iram.fr/IRAMFR/GILDAS/`.

Cologne Database for Molecular Spectroscopy (CDMS). *Molecules in Space.* `http://www.astro.uni-koeln.de/cdms/molecules`.

Hily-Blant, P. et al. (2006). *GILDAS CLASS Documentation.* 1.1. URL: `http://www.iram.fr/IRAMFR/GILDAS/`.

Long Wavelength Array. *Karl G. Jansky and the rotating antenna array.* URL: `http://lwa.phys.unm.edu/history.html`.

M. Richmond. *The Interstellar Medium: Gas.* `http://spiff.rit.edu/classes/phys230/lectures/ism_gas/ism_gas.html`.

MPIfR. *Radio Telescope Effelsberg.* URL: `http://www.mpifr.de/english/radiotelescope/index.html`.

NASA. *Astronomy Picture of the Day.* `http://apod.nasa.gov/apod/ap990511.html`.

R. Simon. *MSX.* URL: `http://irsa.ipac.caltech.edu/applications/MSX/`.

S. J. Carey. *IRDC*. URL: http://web.ipac.caltech.edu/staff/carey/dark/dark.html.

Texas A&M Chemical Engineering Department. *The Ammonia Molecule*. URL: http://alcheme.tamu.edu/?page_id=719.

WolframMathWorld. *Distribution Function*. URL: http://mathworld.wolfram.com/DistributionFunction.html.

Acknowledgements

First of all I would like to thank my supervisor Priv.-Doz. Dr. Henrik Beuther for allowing me to work in his group at the Max-Planck-Institute for Astronomy in Heidelberg. He guided me through this bachelor thesis, taught me a lot about radio astronomy and high-mass star formation.
I would also like to thank the members of his group for intergrating me and making me feel welcome, allowing me to take part in discussions and group meetings. It has given me the opportunity to learn more about the work being done in the group and present research.
Thanks also goes to Priv.-Doz. Dr. Hubert Klahr who has agreed to be the second corrector of this thesis and to take part in the final colloquium.
I also want to thank my other bachelor colleagues, Adriana Pohl, Karina Voggel and Paul Molliere, for creating a good working atmosphere.
A great thanks goes also to my proofreaders Karina Voggel, Vanessa Böhm and Alina Bischoff. Thank you for understanding what I meant and translating it into an English everybody else can understand, too.
Finally, I would like to thank my friends and family for the support they have given me not only over the last few months, but also over the last three years, since I moved to Heidelberg. Without them, I would not have come that far.

Ich versichere hiermit, dass ich diese Bachelorarbeit selbständig verfasst und nur die angegebenen Quellen und Hilfsmittel verwendet habe.

With this, I assure that I have authored this bachelor thesis by my own and used only the named sources and aids.

Heidelberg, den 7. Juli 2011

....
(Unterschrift des Kandidaten)